Crystallography Reports, Vol. 48, Suppl. 1, 2003, pp. S3–S24. Translated from Kristallografiya, Vol. 48, No. 6 (Suppl.), 2003, pp. S7–S29.

DIFFRACTION AND SCATTERING OF IONIZING RADIATIONS

Dedicated to the 60th Anniversary of the Shubnikov Institute of Crystallography, Russian Academy of Sciences

XRSW-Based Structure-Sensitive X-ray Spectroscopy of Condensed Matter

A. M. Afanas'ev, S. I. Zheludeva, B. G. Zakharov, R. M. Imamov, M. V. Kovalchuk, V. G. Kohn, M. V. Kruglov, and Yu. N. Shilin

Shubnikov Institute of Crystallography, Russian Academy of Sciences, Leninskiĭ pr. 59, Moscow, 119333 Russia

e-mail: imamov@ns.crys.ras.ru

Received April 28, 2003

Abstract—The method of studying condensed matter based on X-ray standing waves is described. The method's advantages include its numerous modifications and the possibility to extract mutually complementing specific information by using different channels of inelastic scattering. Various modifications of the method are developed in detail, including measurement of the photoelectron and fluorescent quanta yield and photoelectromotive force. The possible use of Compton scattering and thermal diffuse scattering (TDS) in the studies of electronic vibrational and optical properties of solids is analyzed and examined experimentally as well as the possibilities of the structural studies under the conditions of multibeam diffraction. The method for studying the structure of layer organic and inorganic nanostructures based on the use of long-period X-ray standing waves is suggested. A unique apparatus for measuring inelastic-scattering channels under the conditions of X-ray diffraction is designed and constructed. © *2003 MAIK "Nauka/Interperiodica".*

1. INTRODUCTION

The study of a large number of fundamental and applied problems of physics of condensed matter by X-ray methods was associated for quite a long time with the bulk structure. However, in the last three decades, ever increasing interest has been attracted to samples of small dimensions, where the main role is played by sample surface, i.e., to systems with a relatively small number of atoms. Such systems are studied by various surface-insensitive X-ray methods, but all these methods fail to localize certain atomic species in the upper layers of perfect crystals from which the fluorescent quanta and Auger and photoelectrons are emitted. This situation gave rise to attempts to develop surface-sensitive X-ray diffraction methods. The combination of diffraction and spectroscopy of secondary radiations which are characterized by a small escape depth allows one to extract information on the surface and develop structure-sensitive X-ray spectroscopy. This method, which gives unique information on small variations in the atomic structure of condensed matter, is also applicable to problems of structural diagnostics of subsurface layers of single crystals, multilayer inorganic and organic systems, and localization of impurity atoms in a crystal lattice. Below, we illustrate the possibilities of the method by the results obtained mainly at the Institute of Crystallography of the Russian Academy of Sciences.

2. PHYSICAL FOUNDATIONS OF THE METHOD

The idea underlying the method is rather simple. One has to measure the angular intensity curves for X-ray inelastic-scattering channels under the conditions of strong elastic scattering. Under these conditions, a reflected wave with a relatively large amplitude is generated in a crystal. The coherent superposition of the incident and reflected waves gives rise to generation of an X-ray standing wave (XRSW) whose properties depend on the orientation of the incident beam relative to a sample and manifest themselves in the formation of inelastic-scattering channels. In fact, this signifies the formation of a "scale ruler" in a crystal and above its surface with the scale value of several angstroms. The methods if often referred to as the method of X-ray standing waves (XRSWs) [1, 2].

Specific characteristics of a secondary-radiation yield under the conditions of X-ray diffraction were intensely studied in the 1960s [3–5, 7, 8]. The anoma-

lies of the fluorescence radiation yield [5] and thermal diffuse and Compton scattering (CS) [7, 8] were observed experimentally and explained by generation of X-ray standing waves in the course of X-ray diffraction. In the following studies [9, 10], the pronounced anomalies of photoelectron yield under the conditions of X-ray diffraction were recorded experimentally, which, obviously, reflected the formation of X-ray standing waves and confirmed [11] their high sensitivity to very weak distortions of the crystal structure such that the total displacement of the crystal surface produced by various external factors (i.e., ion implantation) was of the order of a small fraction of interatomic spacings (Fig. 1). A similar situation is also possible in measurements of fluorescence signal from impurity atoms located close to the surface [6]. Moreover, the possibility of detecting the thinnest (tens of nanometers) amorphous layers on the crystal surface was predicted [12].

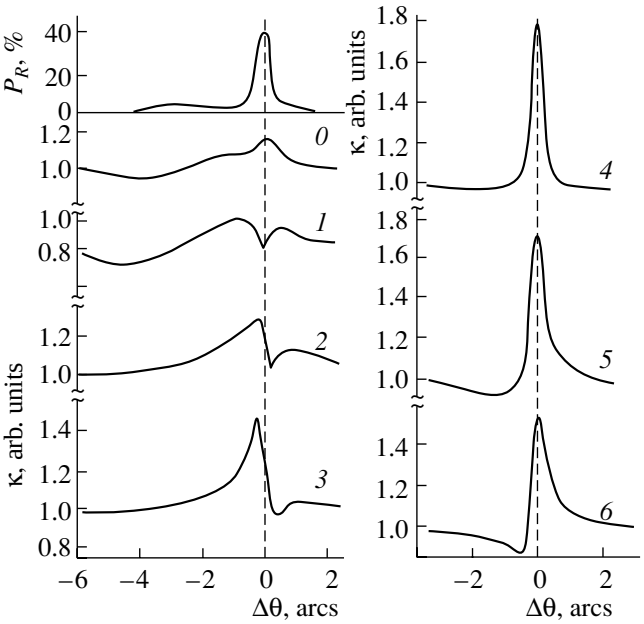

Fig. 1. Experimental angular curves of photoelectron yield in the process of successive removal of the implanted layer. P_R is the diffraction reflection coefficient before etching. Figures on the curves indicate the number of removed 280-Å-thick layers.

The angular dependence of the secondary-radiation yield is described by the general expression obtained in [13], which is valid for photoemission and fluorescence and describes the distortion of the crystal structure in the most general form

$$\kappa_a(\Delta\theta) = \int_0^\infty dz P(z)\kappa_a(z, \Delta\theta), \tag{1}$$

where

$$\begin{aligned}\kappa_a(z, \Delta\theta) &= C[E_0^{i*}(z, \Delta\theta)\chi_{i0}^{il}(a)E_0^l(z, \Delta\theta)\\ &+ E_h^{i*}(z, \Delta\theta)\chi_{i0}^{il}(a)E_h^l(z, \Delta\theta)]\\ &+ 2C\,\mathrm{Re}\{E_0^{i*}(z, \Delta\theta)\chi_{ih}^{il}(a)E_0^l(z, \Delta\theta)\\ &\times \exp[i\varphi(z) - W(z)]\}.\end{aligned} \tag{2}$$

Here, $\varphi(z) = \mathbf{hu}(z)$; $W(z) = \langle(\mathbf{hu})^2\rangle$; $\Delta\theta$ is the angular deviation of the beam from the exact Bragg angle; $P_a(z)$ is the probability of the secondary-radiation yield of type a from the crystal layer located at the depth z; $E_{0,h}(z, \Delta\theta)$ are the amplitudes of the incident (0) and diffracted (H) waves in the crystal; $\mathbf{h}$ is the reciprocal-lattice vector; $\mathbf{u}(z)$ and $W(z)$ are the mean displacement of atoms and the mean-square factor, which describes the weakening of interference because of deformation of the crystal-lattice and atomic thermal vibrations; and C is a constant multiplier. The specific form of the angular dependence of the secondary radiation of type a is determined by the contribution of the corresponding process to the imaginary part of the Fourier component of the polarizability tensor χ_i^{il}. Simultaneous measurements of diffraction reflection curves and photoemission for crystals coated with a thin disturbed layer allow one to reconstruct the factor

$$\begin{aligned}&\langle \exp[i\varphi(z, y)]\rangle\\ &= \frac{1}{L}\int_0^\infty dz P(z)\exp[i\varphi(z) - W(z) + 2iyz/L_{\mathrm{ex}}],\\ &L = \int_0^\infty dz P(z),\end{aligned} \tag{3}$$

which, in the limit $L \longrightarrow 0$, is transformed into $\exp[i\varphi(0) - W(0)]$. Here, $P(z)$ is the probability of escape of photoelectrons from depth z, L is the integral probability of escape of photoelectrons, L_{ext} is the extinction length, and y is the dimensionless parameter of the deviation from the Bragg condition. To describe the function $P(z)$, one uses the well-known empirical formulas of integral probabilities in the form

$$\begin{aligned}P(z) &= \theta(2l - z)(1 - z/2l),\\ l &= 3\times 10^{-6}AE^\gamma/\rho Z, \quad \gamma = 1.3\text{–}1.5,\end{aligned} \tag{4}$$

where ρ is the material density (in g/cm^3), Z is the atomic number, A is the atomic weight, and E is the energy (in keV). In this case, Eq. (3) allows one to reconstruct the disturbance profile directly, i.e., to reconstruct the functions $u(z)$ and $\exp(-W(z))$ over the whole disturbed-layer depth by the method of inverse Fourier transform.

In order to analyze the experimental results, one uses the computer simulation of the experiment for a crystal with an arbitrarily deformed profile of the subsurface layer. The possibilities of this approach were demonstrated in [14]. It was shown that computer simulation drastically reduces the time necessary for the calculation of unknown structural parameters by comparing the experimental results with a set of theoretical curves corresponding to various values of the parameter studied.

Later, the theory was developed for all the inelastic-scattering channels under the conditions of X-ray diffraction [15–32]. It was shown that the Borrmann and Pendellösung effects well known in the dynamical theory of X-ray diffraction manifest themselves differently for different types of secondary radiations, diffraction geometries, and coherence conditions.

Generation of XRSWs in X-ray diffraction influences the photoelectromotive force (photo-emf) arising in X-ray irradiated semiconductors with *p–n* junctions. This phenomenon was first studied in [16] and then, in more detail, in [17]. It was demonstrated that the angular dependence of induced photo-emf is determined mainly by the diffusion lengths L_d of minor carriers in the *p* layer. Depending on the L_d value, the photo-emf curves are similar either to the photoemission curves or the curves of fluorescence yield.

One of the most important problems here is the reconstruction of the profiles of the thinnest (up to atomic layers) disturbed subsurface layers. As follows from the results obtained in [13], the knowledge of the exact value of the function $P(z)$ is necessary for the reliable determination of the parameters of disturbed layers. Empirical Eq. (4) described $P(z)$ only approximately. Therefore, later, a more convenient modification of Eq. (4) for the XRSW methods was suggested [33].

The most appropriate solution of this problem was found in [34]. It was suggested to determine $P(z)$ not in the Bragg geometry conventional for XRSW experiments but in the grazing diffraction scheme of the Laue geometry. The latter scheme does not use samples with disturbed subsurface layers: one determines $P(z)$ in experiments with only one ideal crystal. Thus, the $P(z)$ functions were reconstructed for Si and Ge crystals with photoelectrons from different energy groups [34, 35]. These experiments form the basis for numerous experiments on reconstruction of the profiles of disturbed subsurface layers of crystals.

An important role in the interpretation of physical foundations underlying the method and establishment of its possibilities was played by studies [36–38]. For the first time, the necessity of taking into account the so-called indirect scattering processes was indicated. In this case, the recorded secondary radiation is generated not directly in the field of the standing wave but in more complex cascade processes. Indirect scattering processes do not allow one to use soft Auger electrons in diagnostics of atomic layers on the crystal surface [39].

The possibilities of the method considerably increase if one uses the so-called grazing diffraction scheme. Since the extinction length in this scheme is very small compared to the extinction length in the standard symmetric Bragg scheme, the sensitivity of the method to the thinnest disturbed layers becomes much higher, so that one can readily record disturbed layers as thin as several nanometers. Moreover, the use of the grazing diffraction scheme facilitates the experiment on Compton scattering under the conditions of XRSW formation [19, 20, 22]. In the grazing diffraction scheme, the incoherent part of Compton scattering dramatically increases (Fig. 2), and its separation considerably facilitates the further analysis of the experimental data and gives an absolute point for measurements on the angular scale, which is extremely important for X-ray diffraction measurements [40].

The next step in the development of the method was made in [41]. For the first time, it was suggested to measure the photoemission and fluorescence yield using the coincidence scheme, i.e., to use the two-channel principle. This approach combined the high-resolution photoemission curves (over the depth) and extremely high fluorescence selectivity to the elemental composition of the material.

Unfortunately, the practical development of this approach is hindered by a low transmission of this experimental scheme with respect to the standard variants. We believe that the use of powerful X-ray radiation sources (e.g., synchrotron source) would promote the use of the method in the solution of complex physical problems.

The additional possibilities for localization of atoms in crystals are ensured by measuring the yield of secondary radiations in the multibeam diffraction. The corresponding theoretical analysis was made in [21, 23]; the idea to use the XRSW method without recording inelastic-scattering channels was formulated in [42]. It was suggested to use three-beam diffraction under specific conditions—one of the diffracted beams should have a low intensity. This beam does not affect the interference of strong waves and plays the role of a detector of a standing wave. An attractive feature of this technique is the possibility of changing the effective depth of escape of the secondary process by rotating the crystal.

It should be emphasized that the theoretical and methodological studies resulted not only in deeper understanding of the physical foundations of secondary processes but also in the design of a package of computer programs for numerical simulation of experiments, which, in turn, allowed one to analyze the possibilities of various experimental schemes and determine the structural parameters of the deformed layers by comparing the theoretical and experimental curves of various secondary processes.

3. INSTRUMENTAL IMPLEMENTATION OF THE METHOD

Measurements of various secondary processes induced by an XRSW are rather complex, because the instrument used should provide a high angular accuracy (of the order of fractions of an angular second) and record of various inelastic-scattering channels having different characteristics. At the beginning of the study of secondary processes, our country possessed only a few highly specialized laboratory instruments with rather limited possibilities for research. It was obvious that, for further development of the method and its successful use in practice of physical and materials-science research, it was necessary to design and construct new instruments that could use both standard X-ray tubes and sources of synchrotron radiation.

At the first stage, the most convenient basic instrument proved to be a TRS-1 triple-crystal X-ray spectrometer designed at the Institute of Crystallography [43–45] and manufactured industrially. Because of the high angular sensitivity of this instrument, it was widely used in X-ray diffraction studies.

Later, several precision instruments were designed. They were equipped with collimation and monochromatization blocks, unified multi-circle goniometers, and other devices [45]. These instruments allowed one to use any radiation source and, at the same time, measure diffraction scattering and secondary radiation in any scheme with a high precision. Secondary radiations were measured with the aid of special attachments. The free path of an electron in air is very small; therefore, to record photoelectrons, both crystal and detector should be placed into an evacuated vessel. The general view and the details of the corresponding attachment suggested in [46] are shown in Fig. 3. The attachment consists of two main units—the positioning stage and the working vacuum volume.

The positioning stage provides an arbitrary motion of the crystal in order bring it to the reflection position.

The vacuum volume is an evacuated vertical cylinder closed with the upper and lover flanges. A crystal holder and a photoelectron detector are fixed on the lower flange inside the cylinder.

Along with the above attachment, a special model of the vacuum chamber, which allowed the measurements of photoemission from the entrance and exit surfaces of the crystal in both Bragg and Laue geometries, was designed [47].

Both vacuum attachments have a rather simple design, can be readily constructed, exploited, and modified for work with any goniometer. Electrons are usually detected and integrated by a secondary-emission multiplier. The intensity of electron counting in such measurements is rather low and does not exceed 0.1–0.5% of the intensity of the incident X-ray radiation in different experimental geometries.

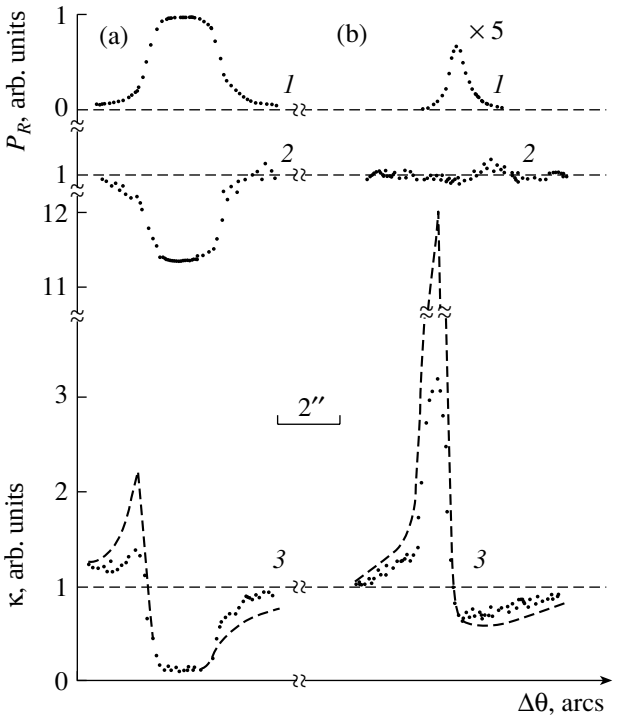

Fig. 2. Angular curves of (*1*) diffraction reflection, (*2*) thermal diffuse scattering, and (*3*) Compton scattering under the conditions of (a) symmetric Bragg diffraction and (b) grazing Bragg–Laue diffraction. The measurements were made on a perfect Si crystal cut out along the [112] direction and forming an angle of 4° with the (111) plane (MoK_α radiation). The dashed line indicates the calculated curve at $\varepsilon_h^{(A)} = \dfrac{\chi_{i0}}{\chi_{ih}} = 0$, where χ_{i0} and χ_{ih} are the imaginary parts of the Fourier components of crystal polarizability.

Photo- and Auger electrons may be recorded by a gas-flow proportional counter [45, 48, 49]. There are several modifications of such a counter, so that it is possible to perform the energy analysis of photoelectrons in the Bragg and Laue diffraction irrespectively of the angle of incidence of X-ray radiation [49] and also under the conditions of multibeam diffraction [45]. The schematic of one such detector [48] is shown in Fig. 4. A counter consists of a cylindrical chamber placed directly onto a goniometer, which allows one to rotate with high precision, which is necessary for measuring diffraction reflection curves. The chamber has special entrance and exit mylar windows. Almost 100% efficiency of photoelectron counting is ensured by a continuous flow of the gas mixture (30% He + 10% CH_4) under atmospheric pressure. The energy resolution of the detector is 18% at the electron energy 8 keV. The resolution was determined from the maximum of photoelectrons formed in the gas as a result of absorption of CuK_α radiation (to exclude photoeffect in a crystal, the incident X-ray beam was parallel to the sample).The above energy resolution of a gas-flow propor-

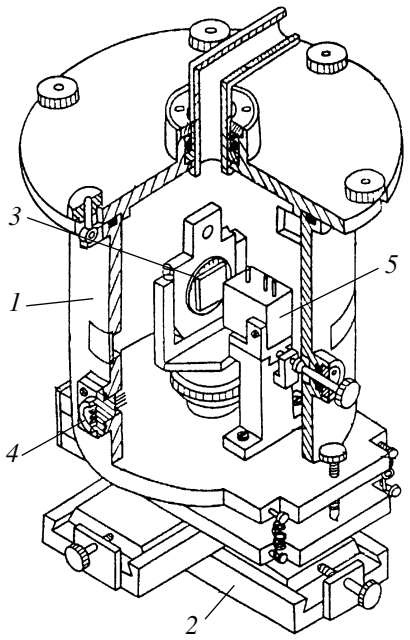

Fig. 3. Vacuum attachment for integral measurements of photoemission induced by an X-ray standing wave. (*1*) Vacuum chamber, (*2*) adjusting stage, (*3*) axis, (*4*) screw, (*5*) translation mechanism.

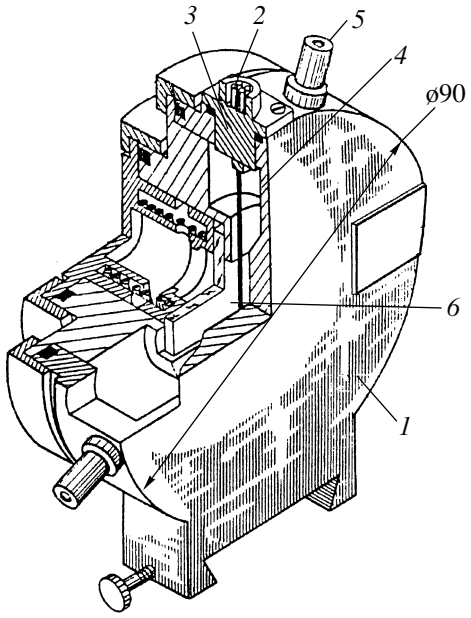

Fig. 4. Schematic of a gas-flow proportional counter of photoelectrons excited by an X-ray standing wave. (*1*) Housing; (*2*) high-voltage connector; (*3*) insulator; (*4*) gold-plated fragment; (*5*) connection; (*6*) sample

tional counter is considered to be rather high. Since the record of photoelectrons by a proportional counter in a gas flow depends on the angle of electron ejection from a crystal, the detector aperture is practically 2π and the integral intensity of counting in this case is much higher than the integral intensity of counting by a secondary-electron multiplier (VEU) (from 1 to 5% of the intensity of the X-ray radiation). Small dimensions, possibility of fast change of samples, high transmission, and the use of the attachment irrespectively of an X-ray diffractometer make gas-flow proportional counters of photoelectrons very convenient instruments for studies of subsurface layers of single crystals by the XRSW method.

In addition to the above gas-flow counter for electron spectrometry, we also designed and constructed energy analyzers of magnetic [50] and electrostatic [51] types with an energy resolution of ≤4% in the vacuum volume.

A higher energy resolution for electrons can be attained by using ultrahigh-vacuum chambers. Using the principle of modules, we designed a high vacuum multicrystal X-ray photoelectron spectrometer [52]. The main module of the instrument is a block of monochromators with two crystals and a vacuum (~10^{-9} torr) chamber with a manipulator and a lock device (Fig. 5). The chamber is equipped with a goniometer with a torsional drive, which allows one to rotate the sample without any clearance within the angular range of about ~10 arcs and a system for energy analysis of photo- and Auger electrons supplied with a 127° cylindrical deflector with a resolution of 1 eV.

The practical use of the XRSW method requires the solution of a number of new problems. Thus, localization of impurity atoms and the analysis of subsurface layers of a crystal with the use of Auger photoelectrons and fluorescence radiation require low-intensity measurements. The time for collecting the necessary statistics can exceed tens of hours with the simultaneous constant precision control of the angular position of a crystal (several hundredths of angular seconds). An increase of the energy resolution of photoelectrons with the aid of magnetic or electrostatic energy analyzers also reduces the signal intensity, so that it is practically impossible to measure the signal by the existing devices. Therefore, in order to accumulate a determined signal, we designed an automatic system of the dynamic control of the angular position of a crystal [50].

The long accumulation (summation) of the signal with averaging of random noise is ensured by multiple scanning of a sample over a narrow angular range corresponding to the range of strong Bragg reflection (from several angular seconds to several tens of angular seconds). On the angular scale, the results obtained in various scanning cycles should coincide with high accuracy. The system has a piezoelectric drive and a multichannel analyzer. A weak signal is accumulated with the aid of two feedback loops. In the first loop, a piezoelectric drive enables an automatic multiple rotation of the sample in the vicinity of the Bragg angle. In the course of the experiment, the drift of the angular

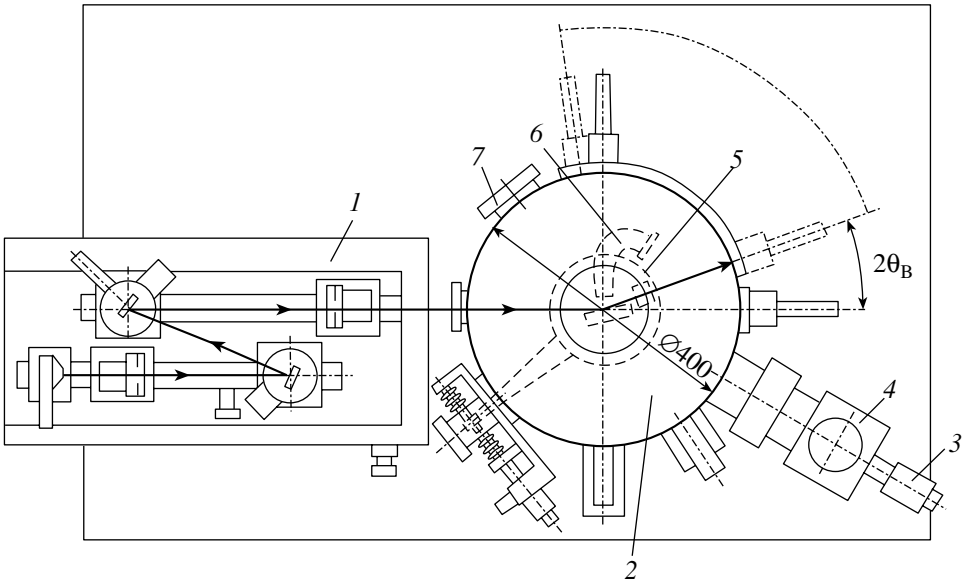

Fig. 5. Schematic of a vacuum spectrometer. (*1*) Block of a two-crystal monochromator, (*2*) vacuum chamber, (*3*) manipulator, (*4*) lock device, (*5*) goniometer with a torsional driver, (*6*) system for energy analysis of photo-signals and Auger electrons, (*7*) viewing window.

position of the crystal is often observed, which is associated with the temperature variation and mechanical instability. The second feedback loop compensates the arising error—it determines the error value and fits the curves after each scanning cycle. The system allows one to accumulate during the experiment a signal with the statistics sufficient for its further treatment.

In order to measure photo-emf from barrier semiconductor structures under the diffraction conditions, a special attachment was designed (Fig. 6) [16] which consists of a metallic base with an insulator plate rigidly fixed in its center and electric connectors for measuring useful signals and supplying the voltage to the *p–n* junction of the crystal studied. The crystal–sample with the ohmic contacts is mounted on an insulated platform and is supplied with connectors to the measuring system. The metal base is covered with a nontransparent metal cap with mylar windows transparent to X-rays. The base is fixed in the head of a crystal–holder of a TRS spectrometer, so that the sample has all the degrees of freedom necessary for bringing it to the reflecting position.

As was indicated in Section 2, the measurements of the photoelectrons and fluorescence yield under the conditions of dynamical X-ray diffraction allow one to perform the layer-by-layer study of distortion of the crystal structure. However, the study of both types of secondary processes in multicomponent crystals encounters serious difficulties; in particular, it is rather difficult to determine positions of the matrix and substitute atoms in the crystal lattice. In order to be able to combine the advantages of both types of radiation—small escape depth of electrons and high spectral resolution of the fluorescence—we measured the yield of both these secondary radiations simultaneously (without allowance for the time of their propagation from the site of their generation to the detector). This is the so-called two-channel method [41]. Here, we used the fact that a photoelectron and a fluorescent quantum generated in one event of photoeffect are related in time. Recording photoemission and fluorescence from the sample and selecting the pair events with the aid of the coincidence scheme (Fig. 7), one can obtain the angular curves of the fluorescence yield of selected atomic species located within the escape depth of photoelectrons.

4. STUDY OF SECONDARY PROCESSES

In this section, we consider the studies of phenomena associated with various types of secondary radiation from a crystal. Numerous examples showed the great potentialities of the method for extracting the information on the parameters of the surface structure of single crystals and thin films and localization of impurity atoms in the vicinity of the surface and in the crystal bulk of various inorganic and organic multilayer nanostructures.

4.1. Electron Photoemission

Attempts to establish experimentally the main laws of electron escape from crystals under the conditions of X-ray dynamic diffraction in various geometries, including several modifications of asymmetric grazing schemes, were made in a large number of studies [1, 2, 14, 26, 32, 38, 53–55]. The possibilities offered by this type of secondary radiation were widely used to study structural distortions of submicron levels in crystals

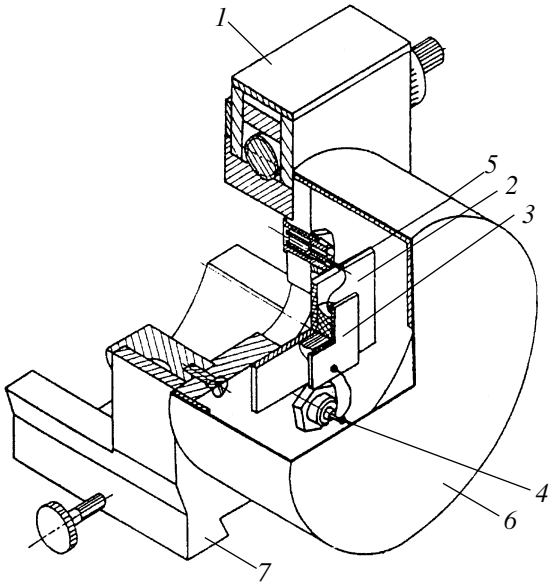

Fig. 6. Schematic of an attachment to the spectrometer for photoelectric measurements under the conditions of X-ray diffraction. (*1*) Crystal holder, (*2*) base insulator for fixation of the sample, (*3*) sample, (*4*, *5*) joints for measuring electric signals, (*6*) light-opaque cap, (*7*) guides for attachment installation on the plate of the main goniometer of a triple-crystal spectrometer.

whose surface was subjected to chemical–mechanical polishing, pulsed laser treatment, reactive ion etching, and ion implantation [32, 49, 56–59].

The method of record of photoelectrons turned out to be the most efficient method for studying distortions of the structure subjected to the finishing treatment. These distortions are observed in a thin subsurface layer where the traditional X-ray methods are insensitive. Thus, the curves of photoelectron yield were used to study the structural distortions in the surface layers of germanium polished by diamond ASM-1 and ASM-3 pastes and subjected to chemical–mechanical polishing [60, 61]. The analysis of the photoelectron yield (Fig. 8) showed that the chemical–mechanical treatment of the surface of a germanium crystal induces small structural distortions in a surface layer whose thickness does not exceed 0.1 μm. Surface polishing by diamond pastes with 1- and 3-μm-large grains results in the formation of a distorted layer whose thickness exceeds 0.3 μm. The subsequent chemical etching to a depth of 0.2 to 0.3 μm changes the curves of photoelectron yield unless their shape becomes similar to the curves of perfect crystals, which indicates the complete removal of the layer distorted by diamond polishing.

The curves of photoelectron yield were also used for studying the process of laser amorphization of gallium arsenide [59]. The curves obtained indicated the presence of a ~300-Å-thick amorphous layer on the laser-irradiated (density of the laser radiation ~0.3 J/cm^2) gallium arsenide surface.

High sensitivity of photoemission curves to deformations in autoepitaxial GaAs, Ge, and Si layers at the initial stages of their growth (where the layer thickness is much less than the extinction length) was demonstrated in [62, 63]. To determine small deformations in thin epitaxial silicon films, the curves of photoelectron yield were recorded from the 444 reflection (CuK_α radiation) [64]. Thus, the problem of increasing the extinction lengths with the aim to satisfy the necessary conditions $L_{el} \ll L_f \ll L_{ext}$ (where L_{el} is the escape depth of photoelectrons, L_f is the film thickness, and L_{ext} is the extinction length) was solved, which allowed one to determine the complete deformation profile of a disturbed layer. The samples studied were Si single crystals doped with Sb up to the concentration 3.7×10^{19} atom/cm^3 and coated with a autoepitaxial silicon film doped with boron up to the concentration 10^{16} atom/cm^3. One film was used as a standard, whereas all the other films were homogeneously doped with germanium to concentrations ranging from 3.7×10^{19} atom/cm^3 to 1.5×10^{20} atom/cm^3. The film thickness was 1.5 μm, whereas the extinction length was L_{ext} = 10.5 μm and L_{ext} = 0.35 μm. The experimental curve of photoelectron yield (Fig. 9) showed the displacement of the surface due to relaxation of the crystal lattice for small fractions of the interplanar spacing. The minimum deformation takes place in the sample described by curve *c* similar to the ideal curve. On the other hand, although curves *a* and *e* are similar, their shapes are inverse with respect to curve *c*. Curves *b* and *d* are characterized by intermediate values. Thus, the shape of photoemission curves allows one to qualitatively determine the degree of deformation in an epitaxial Si film.

The unique information can be obtained by recording photoemission under the conditions of dynamic X-ray diffraction in more complicated multicomponent crystals [57, 65]. Figure 10 shows the experimental photoemission curves for Bragg X-ray diffraction from differently treated gadolinium–gallium garnet (GGG). The analysis of the experimental data shows that the minimum structural distortion of the subsurface layer of a GGG crystal is induced by finishing chemical–mechanical polishing with sol-based silica etchants.

The angular curves of photoemission recorded in the integral mode were used to extract the information on the upper-layer structure of the GaAs/$Ga_{1-x}Al_xAs$ superlattice on a perfect GaAs substrate [66]. The anomalies of the yield characteristic of photoemission allowed us to evaluate the degree of disorder in GaAs and $Ga_{1-x}Al_xAs$ layers.

The possibilities of electron photoemission for diagnostics of subsurface layers of single crystals and films considered above are characteristic of X-ray diffraction in the Bragg geometry and, moreover, of its symmetric variant and the record of the intensity of integral yield of photoelectrons. This is somewhat advantageous for solving applied problems because the method is characterized by high statistics of pulse counting and rather

high sensitivity to the thickness of a disturbed subsurface layer of the crystal.

In fact, the distortions in the subsurface layers of single crystals can also be analyzed rather efficiently using the curves of photoelectron yield obtained in other diffraction geometries. The characteristics of the curves of photoelectron yield in the grazing Laue geometry were first studied in [67]. Rotating a crystal about the reciprocal-lattice vector, we managed to decrease the extinction lengths L_{ext} severalfold and obtain the curves of photoelectron yield from the entrance surface of the crystal. The latter curve had a pronouncedly anomalous shape. High sensitivity of these yield curves obtained in the integral mode to the structural distortions of epitaxial Ge films grown on GaAs substrates and the subsurface GaAs layers was demonstrated elsewhere [68].

The transition to diffraction in the grazing Bragg–Laue geometry [69, 70] increases the possibilities of photoemission of electrons. In this diffraction scheme, the sensitivity of photoemission curves to thin disturbed layers is much higher than in the standard Bragg geometry. Thus, it becomes possible to record amorphous layers as thick as 10 nm or more. Varying the angle of incidence in this scheme, one can implement both symmetric and asymmetric diffraction schemes using only one crystal and also pass from the Bragg to the Laue geometry. The specific characteristic of this scheme is that the extinction length L_{ext} is much less than in the conventional scheme and, therefore, varying the angle of exit of the diffracted beam and the electron energy, one can readily vary the ratio of L_{ext} to L_{el}.

The experiments with the separation of escaped electrons according to their energies allow one to study the structure of the subsurface layer located at a certain depth from the surface [53, 55, 71, 72]. This is illustrated by Fig. 11a, which shows the energy spectrum of photoelectrons from a Si single crystal recorded by a proportional gas-flow counter [71]. The separation of signals from certain energy ranges corresponding to different energy losses of electrons allows one to obtain information on the regions of subsurface layer located at different depths. As was indicated in Section 2, the knowledge of the probability function of escape of photoelectrons, $P(z)$, is desirable for the direct analysis of the structural perfection of surface layers in the range from 0.05 to 1 μm. Figure 11b shows the probability functions $P(z, E)$ for various energy ranges which were determined experimentally by the XRSW method in the scheme of grazing Laue diffraction [34]. The $P(z, E)$ functions thus obtained were used for studying the structural distortions in silicon crystals subjected to multistage ion implantation [73]. As a result, the deformation and amorphization profiles were reconstructed over the whole depth of the disturbed layer.

The above example illustrates the practical solution of the problem of nondestructive layer-by-layer analysis of the structural perfection of the subsurface regions of crystals. The longer accumulation of experimental data or the use of powerful sources of X-ray radiation (e.g., synchrotron radiation) would allow one to measure a larger number of energy ranges, which, in turn, would allow one to increase the number of layers to be studied by a more "dense division" of the subsurface region of the crystal.

In [74], it was first demonstrated that the simultaneous measurement of the angular dependence of X-ray reflection and photoelectron yield over large

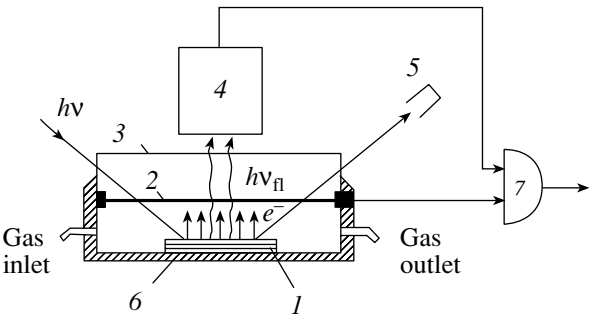

Fig. 7. Schematic illustrating the two-channel XRSW method. (*1*) Sample, (*2*) filament–electrode, (*3*) mylar window, (*4*) semiconductor detector, (*5*) scintillation counter, (*6*) proportional counter, (*7*) coincidence scheme.

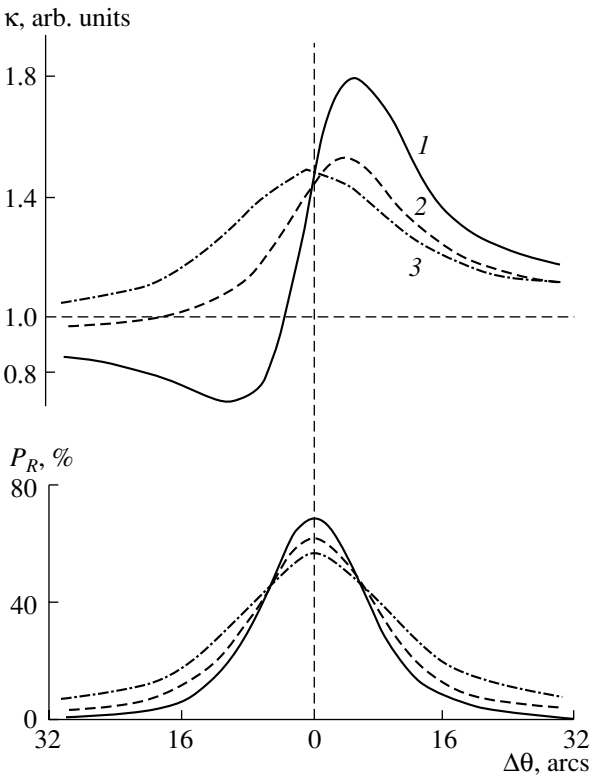

Fig. 8. Simultaneously recorded curves of the angular dependence of photoemission κ and diffraction reflection of differently treated P_R of Ge samples. (220) reflection, CuK_α radiation. (*1*) Chemical–mechanical treatment, (*2*) polishing by ACM-1 diamond paste, (*3*) polishing by the ACM-3 diamond paste.

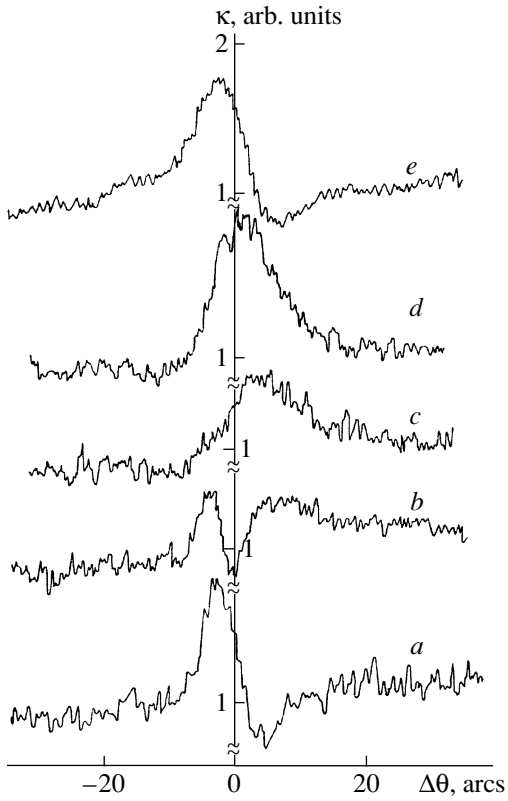

Fig. 9. Angular curves of photoemission from B- and Ge-doped Si single crystals coated with an autoepitaxial Si film at several Ge concentrations. (*a*) Standard, (*b*)–(*e*) samples doped with Ge to the connection from 3.7×10^{19} to 1.5×10^{20} atom/cm^2.

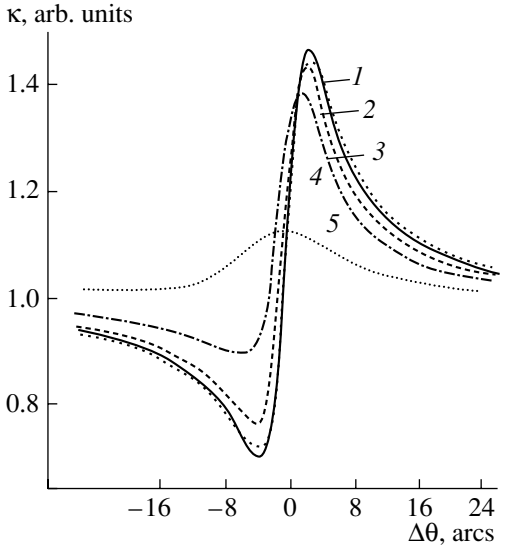

Fig. 10. Experimental angular curves of photoemission from $Gd_3Ga_5O_{12}$ crystals subjected to different surface treatment. 888 reflection, CuK_α radiation. (*1*) Calculation, (*2*) chemical–mechanical polishing by silica sol, (*3*) chemical–mechanical polishing by aerosil, (*4*) chemical–mechanical polishing by aerosil with addition of a diamond powder (soft polisher), (*5*) chemical–mechanical polishing by aerosil with addition of a diamond micropowder (hard polisher).

ranges, including the range of the kinematical diffraction, allows one to measure not only the amplitude but also the phase of the reflected wave. In this case, the structural distortions in the subsurface layer are determined by the method of Fourier transform.

4.2. Record of Fluorescent Radiation under the Conditions of X-ray Diffraction

The yield of fluorescent radiation, $\kappa_\phi(\Delta\theta)$, under the conditions of X-ray diffraction from a one-component perfect crystal in the Bragg geometry gives no new structural information in comparison with the measurements of the X-ray reflection coefficient. This is associated with the fact that, in most instances, the depth of the yield of the fluorescence radiation $L_\phi = 1/\mu_\phi$ exceeds the depth of X-ray penetration into a crystal $L(\Delta\theta) = 1/\mu(\Delta\theta)$, which is equal to the extinction length L_{ext} in the center of the angular range of reflection and the absorption length $L_0 = 1/\mu_0$ at the periphery of the region. This follows from the relationship $\kappa_\phi(\Delta\theta) \approx [1 - P_R(\Delta\theta)]\mu(\Delta\theta)/[\mu(\Delta\theta) + \mu_\phi]$, where $P_R(\Delta\theta)$ is the X-ray reflectivity. Photoelectron emission is characterized by the relationship $\mu(\Delta\theta) \ll \mu_{el}$, whereas fluorescence under the conventional conditions is characterized by the inverse relationship $\mu(\Delta\theta) \gg \mu_\phi$, and the curve of the fluorescence yield coincides with the inverse diffraction reflectivity curve. This fact was confirmed in [75]. However, it was established that an XRSW penetrates the crystal at a certain angle, which results in the local decrease of the fluorescence yield. In the symmetric case, this effect is rather weak, because the region of the lower fluorescence yield coincides with the region of the minimum yield of the secondary signal. In the asymmetric case, these regions are separated, and the above effect is observed quite clearly [19]. The additional characteristics of the fluorescence yield were studied for the case of asymmetric grazing geometry, which allows the easy transition from the Bragg to Laue geometry [20].

The use of a detector of fluorescence radiation with high energy resolution allows one to distinguish the signals from various atomic species, e.g., to single out the signal from impurity atoms incorporated into a perfect crystal. Thus, measuring the signal from As atoms implanted into a silicon crystal [76], we managed to establish that the intensity of the fluorescence yield from As atoms is $\kappa_\phi(\Delta\theta) \approx 1 + P_R(\Delta\theta)$, which indicated the complete disorder in the arrangement of As atoms. This is consistent with the fact that, in this case, the implantation dose exceeded the amorphization limit.

Measuring the fluorescence signal from impurity atoms in X-ray diffraction in the Laue geometry, one can study the correlation in the arrangement of impurity atoms distributed over the whole crystal volume. Such a study was made on a silicon crystal doped with germanium at a dose of 7.5×10^9 atom/cm^3 [77]. The experimental curve obtained was compared with the

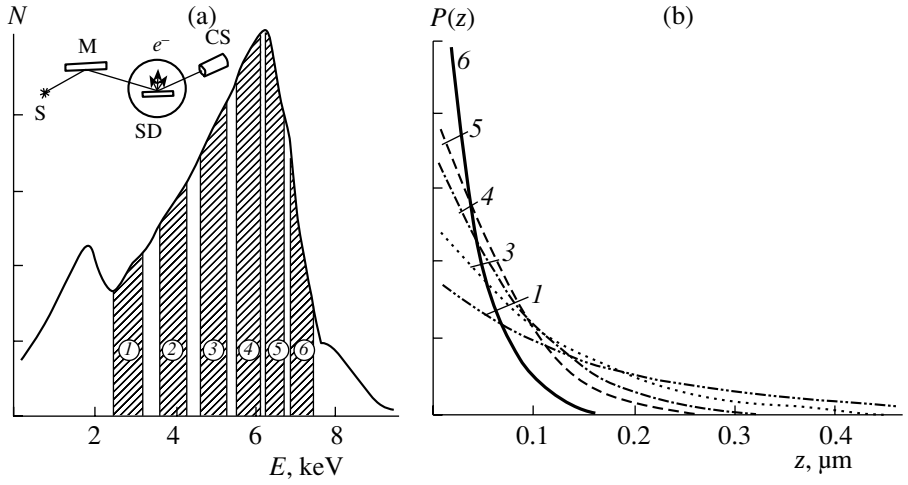

Fig. 11. (a) Energy spectrum of photoelectron yield from Si crystals (CuK_α radiation), schematic of the experiment, and (b) probability function of yield $P(z, E)$ for (*1*)–(*6*) different energy ranges. (*1*)–(*6*) Different ranges of electron energies.

curves calculated under the assumption of the existence or absence of correlations in the arrangements of impurity atoms. It turned out that germanium atoms in this sample occupied the same positions as silicon atoms. The study along this line was continued in [24, 25].

Interesting objects for structure-sensitive fluorescence spectroscopy are garnet crystals with a large number of atoms in their unit cells. The possibilities of the method were studied using the example of gallium–neodymium garnet (GNG) (symmetric (444) reflection, MoK_α radiation) [78]. We measured GaK_α and NdK_α fluorescence yield (Fig. 12). The tails of the fluorescence-yield curves are characterized by different asymmetries, which indicates different arrangements of atoms in the lattice with respect to the XRSW. In this case, the coherent positions of atoms remained unchanged, but their effective coherent fractions were different.

A very promising technique for studying multicomponent crystals (including garnets) is the so-called two-channel method [41], in which the fluorescent signal is measured simultaneously with the photoelectron yield and only the events occurring simultaneously are analyzed. The simultaneous record of a photoelectron and a fluorescent quantum indicated that the atom which emitted the fluorescent quantum was located at a small depth. Despite the low count rate of such quanta, their angular dependence had a structure-sensitive shape. With due regard for selectivity with respect to energy, this fact allowed one to determine the positions of certain atomic species in multicomponent crystals. The method was used to study a single crystal of yttrium–aluminum garnet $Y_3Al_5O_{12}$ (YAG) containing about 5% terbium impurity [79]. Figure 13a shows the experimental curve of the Tb$L_{\alpha,\beta}$ radiation yield obtained by the conventional method. Because of the considerable escape depth of the Tb$L_{\alpha,\beta}$ radiation ($L_\phi \approx 17$ μm), the curve obtained was, in fact, the inverse diffraction reflection curve and gave no information about the arrangement of atoms in the unit cell. Figure 13b shows the curves of the Tb$L_{\alpha,\beta}$ and YK_α radiation yield obtained by the two-channel method. The dashed line shows the curve calculated for terbium atoms in the replacement model, which takes into account indirect excitation [38]. The good agreement of this and experimental curves shows that terbium atoms replace (within the experimental error) yttrium atoms in the unit cell of a YAG crystal.

The arrangement of impurity atoms implanted into a perfect silicon crystal was studied in [80] on a sample doped with iron and nickel atoms ((111) reflection, CuK_α radiation). The diffraction reflection curves and the curves of K_α fluorescence from silicon, iron, and nickel were measured. Like in [76], the impurity atoms in the initial sample turned out to be completely disordered. After sample annealing, the impurity iron atoms had a nonzero coherent fraction $f_c = 0.2$, whereas the variation in the interplanar spacing amounted to $\Delta d/d = -3.8 \times 10^{-4}$.

Similar to the analysis of fluorescence measurements and measurements along other channels of secondary radiation, it is important to know the structure of XRSWs in a bent crystal [81–83]. The calculations showed that the diffraction regions of the angular curves of both reflected X rays and secondary-radiation yield are somewhat broadened, because the wave reflected from the surface may also be reflected from a layer located at a certain depth in the crystal. The interference of the wave reflected at different depths results in noticeable oscillations of the diffraction reflection curves and the curves of the secondary-radiation yield.

The curves of the fluorescence yield were used to identify atomic species in the crystal lattice of the $Cd_{1-x}Zn_xSe_yTe_{1-y}$ solid solution [84]. The zinc and

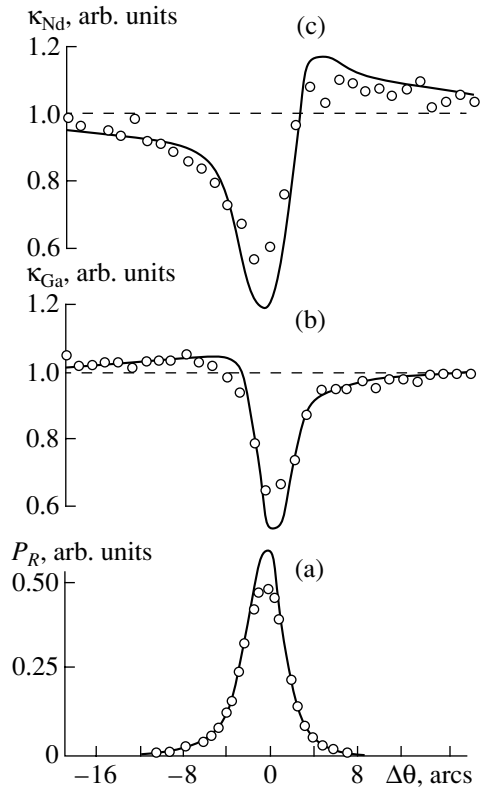

Fig. 12. (a) Diffraction reflection curves of the (444) reflection and (b, c) curves of the of GaK_α and NdK_α fluorescence yield for a perfect neodymium–gallium garnet.

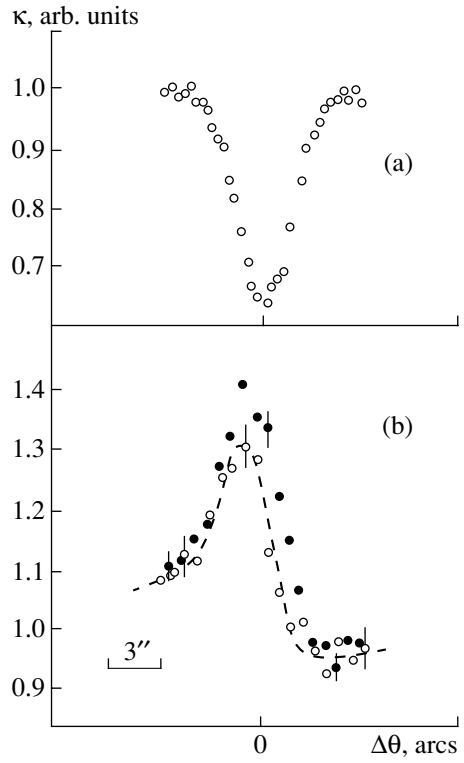

Fig. 13. Curves of TbL_α (circles) and YK_α (dots) fluorescence yield obtained by the (a) standard and (b) two-channel XRSW methods for a YAG crystal (400 reflection, MoK_α radiation); dashed line is the calculation for Tb atoms in the replacement model with due regard for indirect excitation by the YK_α radiation.

selenium contents in the sample were $x = 0.01$ and $y = 0.036$, respectively. The experiments were performed on a source of synchrotron radiation of Cornell University. The energy of X-ray quanta was $E = 13$ keV. The diffraction reflection curves and the SeK_α, ZnK_α, TeL_α, and CdL_α fluorescence yield were measured. To reduce the escape depth of fluorescence, the last was measured by a silicon–lithium detector at a grazing angle of ~2° to the sample surface. The comparison of the measured angular dependences and the results of the computer simulation showed that zinc and selenium atoms occupy the cationic and anionic sublattices, respectively, and confirmed the high perfection of the sample studied.

A more complicated multicomponent system, a film of iron–yttrium garnet with some yttrium atoms being replaced by bismuth atoms, was studied in [85]. The GGG substrates were used. The general chemical formula of the sample was $Y_{3-x}Bi_xFe_5O_{12}//Gd_3Ga_5O_{12}$. Bismuth atoms can replace yttrium atoms in two nonequivalent positions. It turned out that the shape of the diffraction reflection curve only weakly depends on the value of fraction p, whereas the fluorescence curve from bismuth atoms changes its asymmetry at $p = 0$ and 1. We also measured the angular dependence of the fluorescence yield from bismuth, yttrium, and iron atoms (in the film) and gadolinium atoms (in the substrate). The experimental results were in good agreement with the calculated data. As was expected, $p = 0.33$ for yttrium atoms, whereas for bismuth atoms, the curves calculated at $p = 0.44$ fitted the experimental curve much better. Thus, it was shown for the first time that bismuth atoms replace yttrium atoms nonuniformly.

These studies demonstrated high possibilities of the structure-sensitive fluorescence spectroscopy for obtaining information on the arrangement of various atomic species in the crystal lattice of a compound and perfection of the sample structure.

4.3. Characteristics of Other Secondary Processes under the Conditions of Generation of an X-ray Standing Wave

Generation of SXRWs under the conditions of dynamic X-ray diffraction in a perfect crystal influences all the processes associated with excitation of atoms by an X-ray radiation. Along with photoemission and fluorescence discussed above, this is also well seen on photoelectromotive force (photo-emf). Photoelectron absorption of X-ray quanta is accompanied by escape of electrons with certain energy from the atoms.

Some electrons generated in the vicinity of the crystal surface escape from the crystal and are recorded directly by a detector. This process underlies the photoemission method. The other electrons that remain in the crystal cannot be measured directly. Nevertheless, the change in electron concentration affects many electrophysical processes.

Thus, the angular dependence of photoconductivity in semiconductor crystals is changed, and, in the crystals with a *p–n* junction, an anomalous angular dependence of photo-emf arises. The systematic study of these processes under the conditions of the dynamic X-ray diffraction, the so-called internal photoeffect, was performed in [16, 17, 86–89]. According to the general theory of the description of the angular curves of various secondary processes (1), the experimentally measured angular dependence is described by the expression

$$U(\Delta\theta) = \sum_s \int_0^t dz P(z) \frac{dN^{(s)}(z, \Delta\theta)}{dz}, \qquad (5)$$

where the superscript *s* indicates one of two possible polarization states of an X-ray wave, integration is performed along the coordinate axis normal to the surface of a sample having the shape of a plate, and *t* is the plate thickness. Here, the function $N^{(s)}(z, \Delta\theta)$ describes the number of photons absorbed by the atoms in a layer of thickness *z* in the vicinity of the surface at the given angular position of an X-ray beam, $\Delta\theta$, with respect to the Bragg angle. In the case of photo-emf, the $P(z)$ function in the most complete form was derived in [17], where it was shown that, in the particular case where the depth *d* of the location of the *p–n* junction is much less that the penetration depth of X-rays, the upper layer of the *p–n* junction only slightly affects the signal measured. Moreover, as a rule, $t \gg d$, and for the lower layer, the approximation $P(z) = P_0 \exp[-\mu_e(z - d)]$ is valid with a good accuracy. Thus, in this case, $P(z)$ has an approximately exponential form like for the two main channels considered above. The role of the escape depth is played by the diffusion length of minor carriers. This situation can take place both for diffraction in the Bragg geometry, where the reflected beam does not penetrate deeply into the sample, and for diffraction in the Laue geometry, where both beams are transmitted by the plate. In the latter case, the wave field is the superposition of two XRSWs, one of which is also weakly absorbed. This introduces specific features into the angular dependence of photo-emf measured. However, it should be noted that, in experiments, the samples with both thin and thick upper layers of the *p–n* junction were studied. Both layers of the *p–n* junction can give considerable contributions, thus making the situation more complicated.

The main measurements were made on boron-doped *p*-type silicon single crystals. The experiments showed that, with an increase of the thickness of the upper layer of the *p–n* junction and the diffusion length of minor carriers, the signal outside the angular range of diffraction considerably increases, whereas the signal inside this range varies to a lesser degree (Fig. 14). As a result, the angular curve acquires a deep minimum. In the opposite case, one can observe the asymmetric curve against the background of a weaker signal. Here, the angular dependence of the phase of the reflection amplitude manifests itself more pronouncedly. In the case of the Laue geometry, the asymmetry of the curve depends on the location of the *p–n* junction (in the vicinity of the entrance or exit surface).

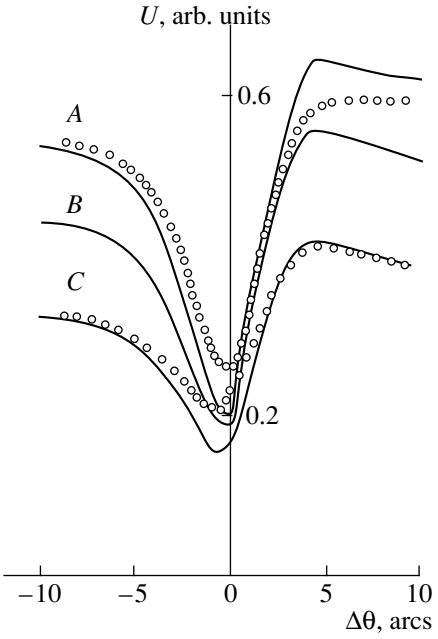

Fig. 14. Theoretically calculated and experimentally measured angular curves of photo-emf under the conditions of X-ray diffraction in the Bragg geometry at various thicknesses of the upper *n* layer in a silicon crystal with the *p–n* junction, (*A*) 20, (*B*) 10, (*C*) 1 μm.

Although the main studies of photo-emf were made on perfect crystals, one can also use this secondary process to record the variation of the scattering parameters of the sample deformation experimentally. This was demonstrated for a boron-doped (10^{16} atom/cm^3) silicon sample, where diffusion of phosphorus (10^{21} atom/cm^3) to a depth of 0.5 μm [89] was observed. Then, the diffusion layer of a part of the sample was etched away. Thus, the sample was deformed in such a way that its curvature continuously varied and increased with an increase of the distance from the boundary of the diffusion layer. The angular curves of photo-emf measured from different exposed regions of the sample surface under the conditions of (111) diffraction of the CuK_α radiation are shown in Fig. 15. The considerable variation of both background signal and shape of the angular dependence are associated, first and foremost, with the variation of the diffusion length

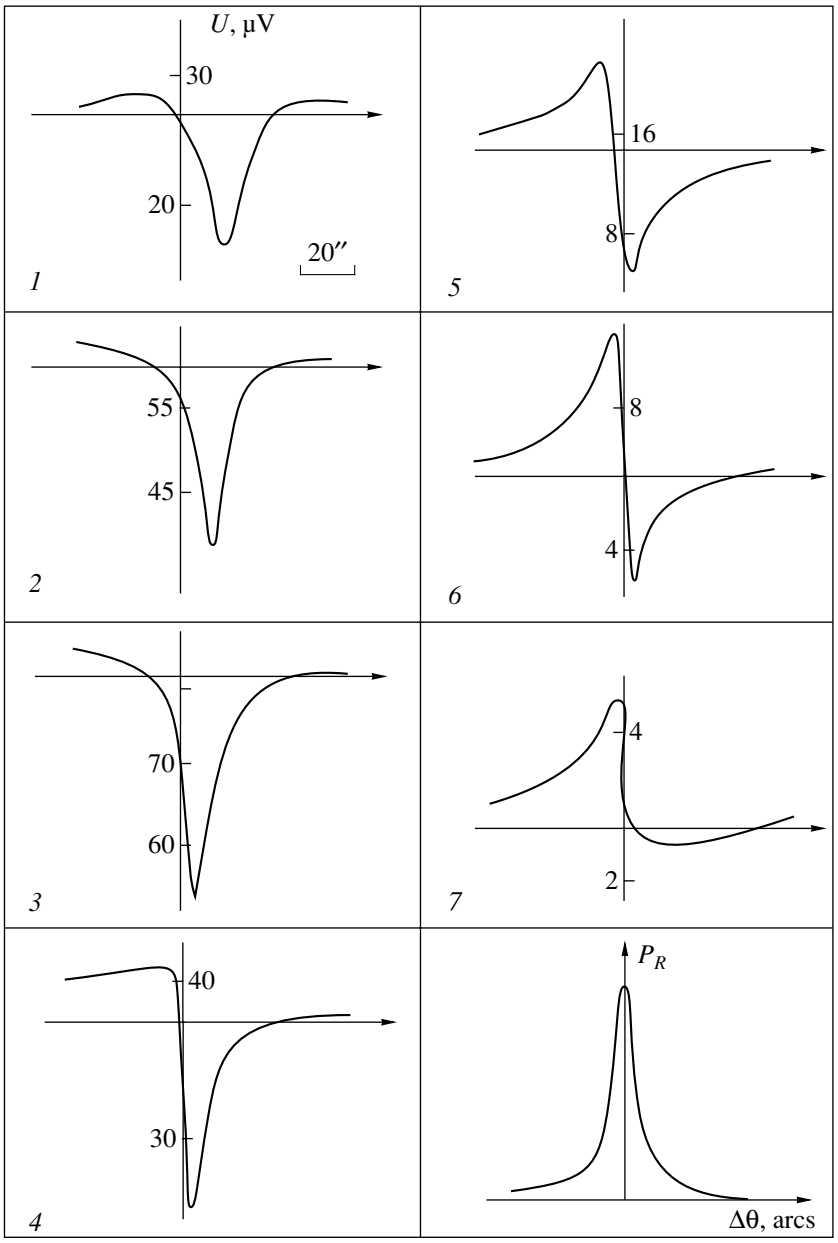

Fig. 15. Angular curves of photo-emf under the conditions of X-ray diffraction measured at the exposure various points of the sample surface and the reflection coefficient of an X-ray beam, P_R. (*1–7*) Different regions of the sample

of minor carriers during deformation and also with the change of nonuniform shift of the nodes and antinodes of an SXRW with respect to the atomic planes.

For other secondary processes such as thermal diffuse scattering and Compton scattering [15, 18, 22, 25, 31, 40, 90–92), the function $P(z)$ has a rigorous exponential form because the secondary process is emission of X-ray radiation of different frequency. However, the nature of the interaction of the electron density of the crystal and the field of an XRSW substantially differs from the case of photoelectron absorption. The main contribution to the intensity of Compton scattering comes from weakly bound valence electrons distributed over the whole crystal, whereas the intensity of thermal diffuse scattering is determined by scattering from electrons vibrating together with atoms, with some part of the energy and pulse of the incident photons being given to the crystal lattice as a whole. At the same time, the common features of the angular dependence are determined, first and foremost, by the structure of the wave field which is the same for all the secondary processes.

Thus, the curves of the angular dependence of the Compton effect in the case of Laue diffraction in thin and thick samples measured in [91] change their asymmetries similar to the angular curves of photo-emf measured in [17]. At the same time, fine details of these

curves allow one to reveal the specific parameters of the interaction studied. In the Bragg geometry, the pronounced extinction results in the formation of a deep minimum in the center of the region of total reflection similar to the fluorescent radiation, but at the periphery of this region, one observes the asymmetry opposite to that observed for fluorescence.

The theory of the yield of Compton and thermal diffuse scattering developed in the studies reviewed above describes the specific features of the processes quite well. These processes are described by various yield curves at different ratios of the matrix elements of the susceptibility tensor, since their formation is influenced by many different parameters.

4.4. Study of Inorganic and Organic Layer Nanostructures Using Long-Period X-ray Standing Waves (LPXRSW)

The development of planar nanotechnology allows one to grow various inorganic and organic ultrathin layers and use them to create absolutely new systems possessing interesting physical properties. Thus, the Langmuir–Blodgett method allows one to obtain molecular layers and nanostructures widely used in molecular electronics and biotechnology. The adequate characterization of such objects required the search for new XRSW generators with a period commensurate with the characteristic dimensions of the structures studied (tens of angstroms). Long-period XRSWs are generated in layer structures with a certain period under the conditions of Bragg diffraction and above the surface of the reflecting mirror in the region of total external reflection.

In the region of total external reflection, the wave field is an XRSW formed as a result of the coherent superposition of two waves with equal intensities with the period $D_{stw} = \lambda/2\theta$, where λ is the wave length and θ is the angle of incidence of the primary beam. With an increase of θ, a decrease in the XRSW period results in its "compression" and its shift toward the surface.

The main advantages of artificial periodic multilayer structures (PMS) as generators of long-period XRSWs in the range of Bragg diffraction are a rather large controllable period, relatively pronounced reflection (%), considerable width of the diffraction maximum, and possibility of preparing periodic multilayer structures with a given composition and surface. This, in turn, allows one to generate an XRSW which, unlike an XRSW in conventional crystals, has a period ranging within 10–100 Å.

Based on the recurrent relation, we considered theoretically the effects of dynamic diffraction in periodic nanostructures and the specific features of formation of wave fields in the region of total external reflection in layer systems, including waveguide ones [93]. We also suggested the scheme for calculating the reflection coefficients and the yield curves of secondary radiations, which were then used to write a complex of computer programs for numerical simulation and analysis of experimental data.

The specific features of the formation of an XRSW in a periodic multilayer structure under the conditions of Bragg diffraction and in Langmuir–Blodgett layers were studied experimentally with the use of fluorescence and photoemission in [94, 95].

If a periodic structure is used as a generator of XRSWs for studying the surface layers, a more stable PMS is more preferable; it allows one to obtain a well developed XRSW with the controllable parameters. This was proved experimentally for an organic structure consisting of 11 $PbSt_2$ bilayers applied onto the Rh/C periodic multilayer structure with a period close to the period of $PbSt_2$ (~59 Å) [96, 97], which is known to generate an XRSW. It was established that a small mismatch of the periods of a Langmuir–Blodgett film and a periodic multilayer structure allows one to extract structural information on an organic layer. Thus, we managed to experimentally determine the tilt of hydrocarbon chains of organic molecules (~27°) and the thickness of the transition layer between the Langmuir–Blodgett film and the MPC (of the order of several angstroms, depending on the sample region considered).

Combining the measurements made by the XRSW method under the conditions of Bragg diffraction in PMS and fluorescence measurements of the film under total external reflection, we developed a new method for determining the thicknesses of ultrathin layers in the case where the layer thickness is much less than the XRSW period. This allowed us to use a PMS as a generator of a long-period XRSW compared to that in an ideal crystal. The role of the coherent fraction was played by the film thickness, and the role of the coherent position, by the parameter characterizing the displacement of the film with respect to the surface of the periodic multilayer structure. If the thickness is known, the film density is determined from the curves of fluorescence yield in the region of total external reflection.

The method was also used to determine the thicknesses and densities of ultrathin iron films [7, 8]. The sample was an iron film obtained by laser sputtering onto the Rh/C periodic multilayer structure ($D \sim 59$ Å, $d_{Rh} = 10$ Å, $N = 20$). The upper layer of the MPC consisted of carbon. An iron film was deposited onto two regions of the sample, (1) and (2); then, region (2) was also coated with a carbon layer. The experimental and calculated data for the case where an XRSW is formed in the Rh/C PMS under the conditions of Bragg diffraction and modulates the fluorescence yield from the Fe film are shown in Fig. 16. The shape of the angular dependence of the fluorescence yield shows that both open and protected iron films have different thicknesses. Processing of the experimental data gave the thicknesses 36 ± 3 Å and 22 ± 3 Å, respectively. The interaction of the iron film with the atmosphere results in the formation of iron oxide and hydroxide and film expansion. The measurements from region (1) in the

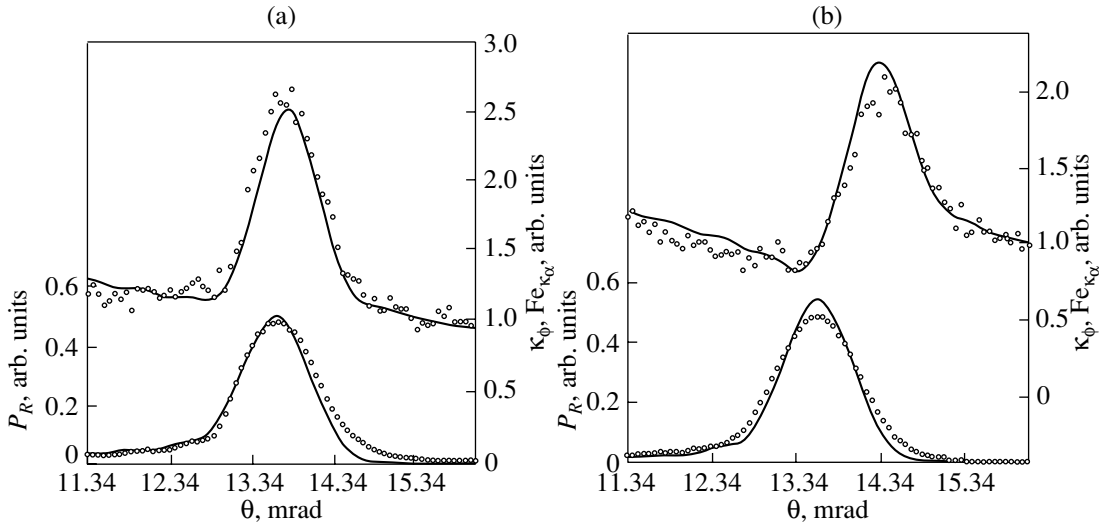

Fig. 16. Angular curves of fluorescence yield from Fe film and the diffraction reflection curves for samples (a) and (b) in the range of Bragg diffraction. Dots indicate the experimental results.

region of total external reflection showed that the best agreement between the theory and experiment is obtained at a density of the iron film, ρ, of ~45 ± 5% of ρ_0 (a tabulated value for a bulk sample). For a film coated with carbon layer (2), the ρ value was (~85 ± 5%)ρ_0.

Based on the record of the characteristic fluorescent radiation in the region of total external reflection, the method of determining the positions of heavy atoms in molecular Langmuir–Blodgett films was developed. The model experiments [99] showed how the complicated distribution of wave field intensity varies in the vacuum/film/substrate system. This variation results in the modulation of the angular curves of the fluorescence yield from heavy atoms in the Langmuir–Blodgett structure, which, in turn, allows one to determine the positions of such ions along the surface normal of the substrate. Here, the following situations can be observed: the situation where ions form a continuous layer on the surface (it is also possible to evaluate its thickness and the position with respect to the reflecting mirror), the situation where these ions penetrate the Langmuir–Blodgett film and occupy the heads of organic molecules, and the situation where these ions form clusters in the Langmuir–Blodgett films.

Thus, in the experiments on characterization of the interface in a Langmuir–Blodgett heterostructure, the sample was a Langmuir–Blodgett film consisting of eight stearic acid monolayers (four ~50-Å-thick periods) deposited onto a plane hydrophobic Si substrate. Then, a lead stearate bilayer was deposited onto the sample (Fig. 17a). For this model experiment illustrated by Fig. 17a, the thickness of the Langmuir–Blodgett films was selected to be ~50 × 6 ~ 300 Å. At this thickness, the second antinode of an XRSW at θ_{cSi} lies in the vicinity of the heads of the molecules forming the upper bilayer (D_{XRSW} ~ 200 Å), which should lead to the passage of nodes I and II of the XRSW through the upper bilayer. Figure 17 shows the calculated angular dependence of the fluorescence yield from Pb^{++} ions located in the heads of organic molecules of the upper bilayer (curve *1*). With an increase in the thickness of the part of the sample that incorporated lead (curves *2*–*5*), which becomes comparable with the period of an XRSW, the shape of the curve of fluorescence yield becomes different. The dots in Fig. 17a correspond to the experimental results which agree well with the curve calculated for the case where the Pb^{++} ions occupy the heads of organic molecules in all five bilayers of the Langmuir–Blodgett film.

Using the method developed in [100–102], we studied the penetration of K^+ ions into a synthetic membrane based on the mixture of the salt of a fatty acid and valinomicin (a membrane-active antibiotic) prepared by the Langmuir–Blodgett method. It is shown that K^+ ions form clusters by occupying channels whose number is determined by the valinomicin concentration. The data obtained agree with the results obtained for a similar system by other methods (Fig. 17b).

The study of X-ray waveguide layer structures by the long-period XRSW method allowed one to determine parameters of individual layers forming the structure and revealed the existence of transition layers at the interfaces [103–107]. We also managed to establish the role of individual layers in the waveguide effects and showed that the minimum thickness of the waveguide cavity is determined by the period of an XRSW formed in it under the conditions of total external reflection when the incidence angle is equal to the critical one [108]. We also studied the dynamics of the variation of the shape of the diffraction reflection curve from the complex multilayer system associated with the formation of the waveguide modes [109, 110] as a result of the change in the resonance-cavity thickness.

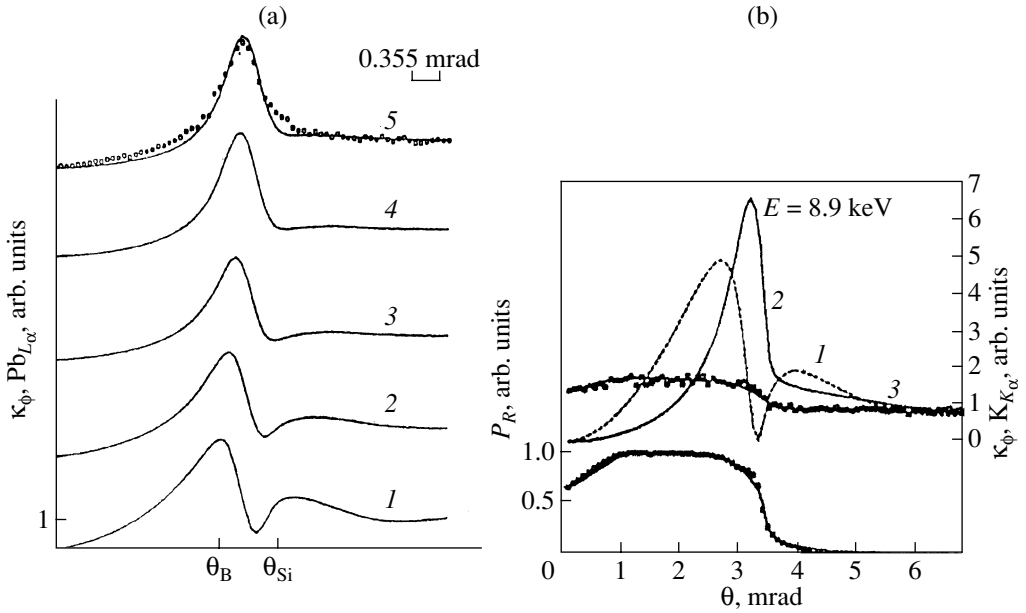

Fig. 17. (a) Calculated angular curves of the Pb L_α fluorescence yield for various distribution of Pb^{++} ions in the Langmuir–Blodgett structure. (*1*) Pb^{++} ions are located in the heads of organic molecules in the upper bilayer of the sample; (*2*)–(*5*) are the curves for samples with increasing thicknesses; (b) X-ray reflection (the lower curve) and K_{K_α} fluorescence for three different distributions of K^+ ions: (1) ions form a thin surface layer, (2) ions occupy at the heads of organic molecules, (3) ions form clusters. Dots indicate experimental results.

Considering monolayers of salts of fatty acid and phospholipids, we showed that the use of waveguide layer structures as substrates for organic monolayers enables one to increase the spatial resolution along the surface normal due to the modulation of an XRSW amplitude in the formation of the waveguide modes. It is proved experimentally that such an XRSW really exists above the surface of the structure consisting of ultrathin metal–carbon–metal layers.

Thus, the methods considered above allow one to extract valuable information on the structure and parameters of artificial ordered systems. We also suggested the methods of obtaining the information on individual layers of the multilayer structure, the variation of their parameters under the action of various external factors, the interfaces in the objects used in molecular electronics, etc.

4.5. Two-Dimensional X-ray Standing Waves under Conditions of Multibeam Diffraction

Multibeam X-ray diffraction is a more complicated method in both theoretical and experimental aspects. In this case, diffraction of an incident plane wave occurs simultaneously from a number of atomic planes and, therefore, we have several diffracted waves and, as a result, a two- or even three-dimensionally periodic XRSW is generated. The location of nodes and antinodes of this XRSW depends on the angular position of the incident beam in two mutually perpendicular planes. Experimentally, one has to collimate an incident beam along two mutually perpendicular planes with an accuracy less than one angular second. The calculation of the parameters of the diffracted waves also becomes more complicated because it requires the diagonalization of a complex matrix of the sixth order in the three-beam case and a matrix of a higher order if there are more than three beams (a problem that cannot be solved analytically). However, the general principles of the theory of the secondary-radiation yield remain the same and should be generalized only formally. The foundations of the theory of the yield of secondary radiations under the conditions of multibeam diffraction were developed elsewhere [111–114]. The number of secondary-radiation quanta is determined from the formula

$$\kappa(\Delta\theta) = C\int_0^t dz P(z)\frac{dN(z,\Delta\theta)}{dz}, \qquad (6)$$

where C is a constant multiplier, which characterizes the value of the signal measured experimentally and, thus, does not affect its angular dependence. The density of the number of the X-ray quanta absorbed in the layer located at depth z is determined from a more complicated expression:

$$\frac{dN(z,\Delta\theta)}{dz} = \frac{1}{8\pi\hbar}\sum_{mm',ss'} E^*_{ms}(z,\Delta\theta)\chi^{ss'}_{imm'}E_{m's'}(z,\Delta\theta)f_{mm'}(z), \qquad (7)$$

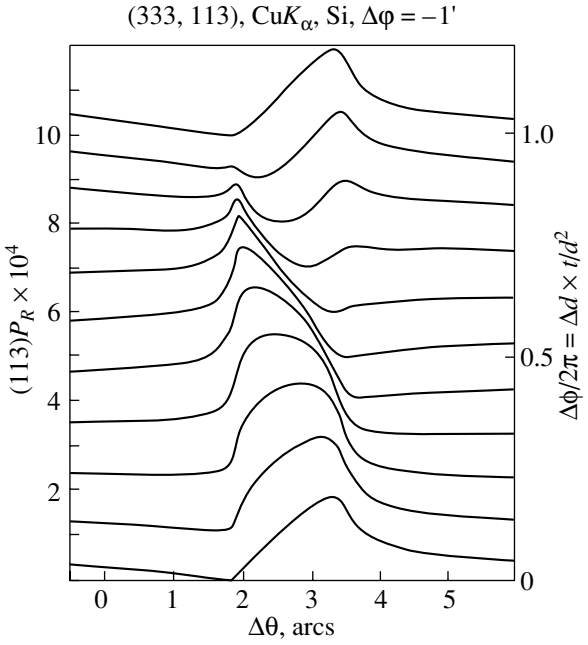

Fig. 18. Angular dependence of the yield of a weak 113 diffracted reflection (Si crystal, CuK_α radiation, $\Delta\varphi = -1'$).

where $E_{ms}(z, \Delta\theta)$ are depth-dependent amplitudes of diffracted waves in a certain polarization state, which are calculated in terms of the normalized eigenvectors of the scattering matrix; the subscript m enumerates the diffracted waves, including the transmitted one, and the subscript s indicates one of two possible polarization states of each wave; and the matrix $\chi^{ss'}_{imm'}$ is a part of the full scattering matrix corresponding to absorption (the components of the tensor of the imaginary part of polarizability convoluted with the polarization vector). Similar to factor (3), the factor

$$f_{mm'}(z) = \exp[-i(\mathbf{h}_m - \mathbf{h}_{m'})\mathbf{u}(z) - W_{mm'}(z)],$$

$$W_{mm'}(z) = \langle([\mathbf{h}_m - \mathbf{h}_{m'}]\Delta\mathbf{u}_a)^2\rangle,$$

describes the phase multiplier.

This direction of the spectrum-sensitive spectroscopy is at the very beginning of its development and, therefore, the numerical simulation and experiments were performed only for photoelectron emission. The data calculated for a perfect crystal and a crystal whose exit surface was coated with an amorphous film in the Laue geometry showed the high sensitivity of the method of two-dimensional XRSWs.

A new modification of the XRSW method with the use of three-beam X-ray diffraction was suggested in [113, 114]. In the angular range where one of the diffracted beams has a low intensity, the effect produced by this beam on other beams is negligibly small. On the other hand, this low-intensity diffracted beam is influenced by two strong beams with due regard for their interference. Thus, a weak diffracted beam plays the role of a new channel of the XRSW method which is independent of inelastic processes and does not require any additional specially designed detector. It was shown that the effective escape depth of this secondary process depends on the angular deviation of a weak beam from the exact Bragg condition [115–118]. The more pronounced the angular deviation, the less its effective escape depth and the higher the sensitivity to deformations in the subsurface layer. Figure 18 shows several curves of the angular dependence of the (113) reflection in the case of three-beam (333, 113) diffraction of the CuK_α radiation in a 1-μm-thick silicon crystal coated with an epitaxial film. The angular range corresponds to the strong (333) reflection in which the

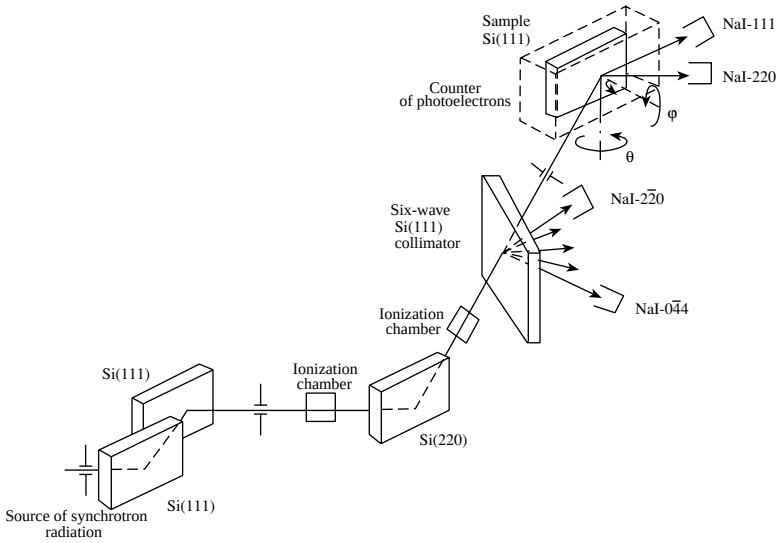

Fig. 19. X-ray optical scheme of a multibeam experiment with the use of a six-wave collimator.

reciprocal-lattice vector is perpendicular to the crystal surface. Different curves correspond to different values of interplanar spacings in the film and in the substrate. As a result, the crystal surface is displaced with respect to nodes and antinodes of an XRSW by a value ranging from zero to the XRSW period (the phase of the reflected wave varies from zero to 2π). Like in the case of photoemission curve, the shape of the diffraction reflection curve of a weak beam is also changed in several stages.

The first experiments based on the use of this modification of the XRSW method were performed on a synchrotron radiation source at the Tsukuba Photon Factory Japan [115, 116]. The role of a two-dimensional collimator was played by the effect of anomalous transmission in six-beam X-ray diffraction (Fig. 19), which was predicted theoretically and was studied experimentally for the first time in the same series of experiments. As a result of anomalous transmission, a thick silicon crystal transmitted a true plane wave whose angular position satisfied the Bragg conditions. A sample was rotated about two mutually perpendicular axes, which allowed one to record the two-dimensional (θ and φ, where φ is the deviation from the multibeam position) angular dependence of the diffracted beams. The experimental data on photoelectron yield from a perfect silicon crystal in the case of (111/220) three-beam diffraction (the radiation wave length $\lambda = 0.115$ nm) were compared with the results of numerical simulation (Fig. 20) [115, 117–119]. These data were in good agreement. This experiment opens a new research direction. An important prerequisite of its development is a dramatic increase in computer power and the development of new sources of synchrotron radiation.

We also performed phase-sensitive measurements corresponding to the XRSW method without secondary radiations [116]. Using the same experimental scheme, we recorded the intensity curves of the angular dependence of a weak diffracted beam whose shape was similar to the curves of photoelectron yield. The calculated data were in good agreement with the experimental results (Fig. 21). The next step was made in [120]. The measurements were made on a silicon sample with the deformed subsurface layer formed due to ion implantation made with the aim to study the four-beam case (400/311/111, $\lambda = 0.11$ nm) at the DRAL station of the synchrotron radiation source (Daresbury, England). The measured curve of the angular dependence of a weak beam had a shape inverse to the shape of the curve for an ideal crystal. This experiment clearly demonstrated the possibilities of the new method for studying deformed layers on the surface of single crystals.

The studies considered in this section are unique and have no analogues abroad. These studies lay the foun-

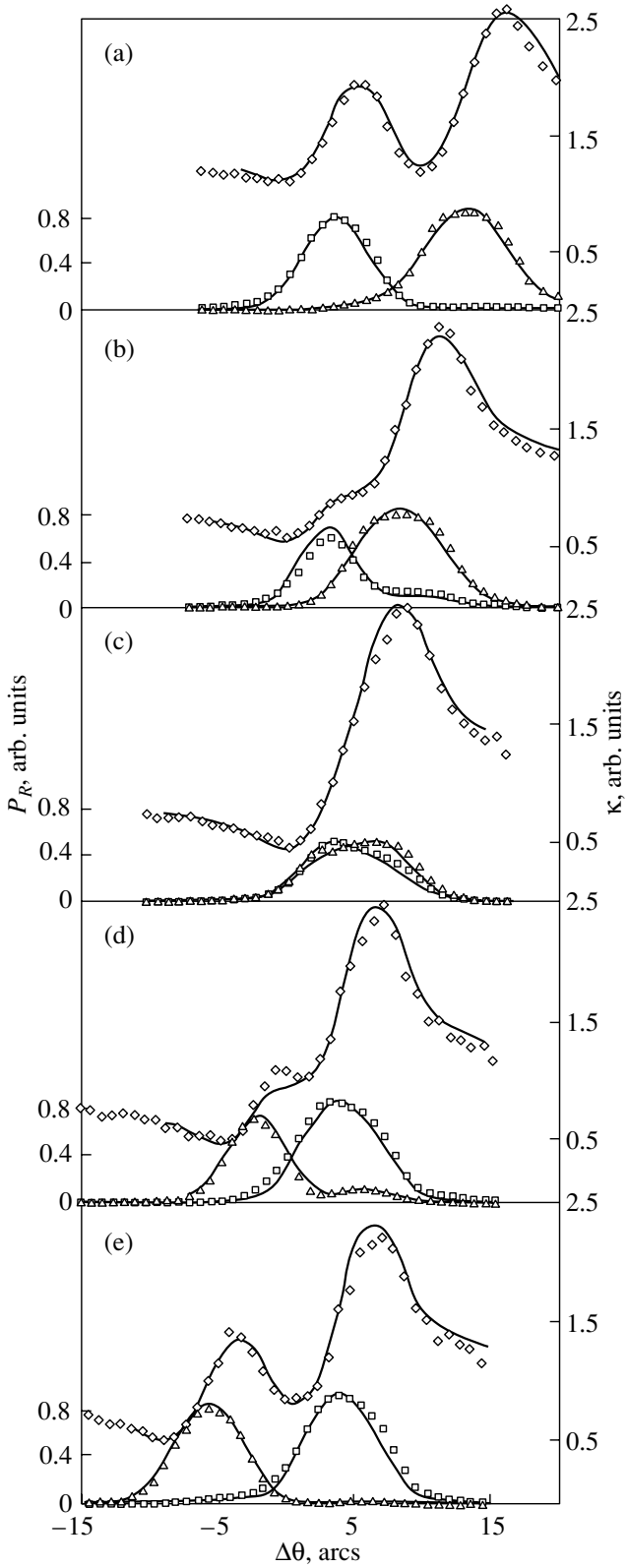

Fig. 20. Diffraction reflection curves and curves of photoelectron yield for various $\Delta\varphi$ values: (a) 12.8″, (b) 7″, (c) 0.5″, (d) 5.3″, (e) 12″. Squares correspond to the 111 reflection; triangles, to 220 reflection; and rhombuses, to the photoelectron yield.

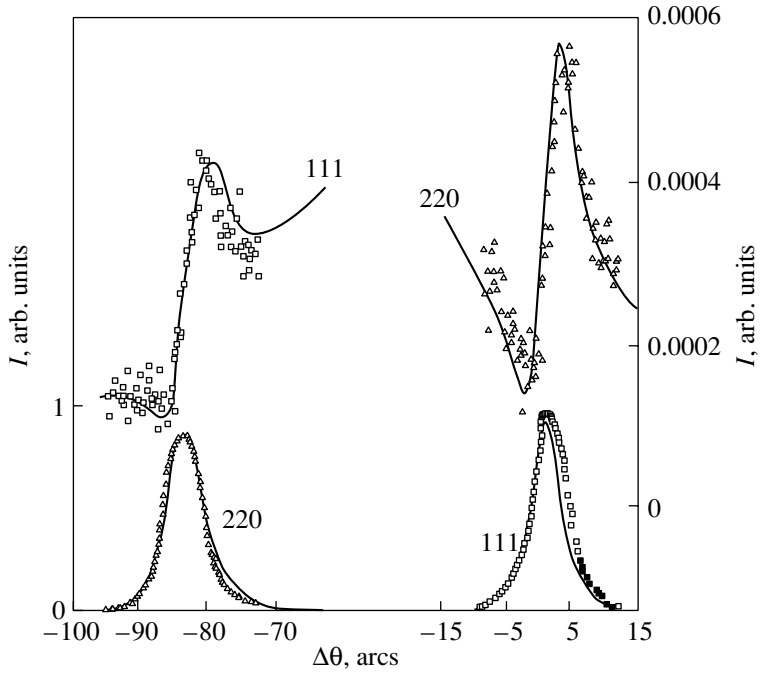

Fig. 21. Angular dependence of the intensities of the tails of the diffraction reflection curves (111) and (220) in the angular region of total external reflection (220) and (111), respectively.

dation for a new promising direction of development of the method.

5. CONCLUSIONS

Thus, the foundations of the experimental study of condensed media using the secondary radiation under the conditions of generation of X-ray standing waves—structure-sensitive X-ray spectroscopy—have been laid. In the course of our studies, a number of scientifically and technologically important results were obtained. The most important ones are the development of the general theory of secondary radiation yield under the conditions of dynamic X-ray diffraction and the experimental measurements of this radiation; the development and design of a new generation of world class precision X-ray equipment with various unique attachments for observation of secondary processes (this equipment is the experimental basis for studying inelastic scattering channels); the design and development of new methods of control of weak distortions of the crystal structure in modern materials, which are important for the solution of various fundamental and applied problems; determination of the positions of impurity atoms in multicomponent (including lasing) crystals; development and practical implementation of a new method of determining the thicknesses and densities of nanodimensional films based on the use of a multilayer periodic structure as a generator of long-period X-ray standing waves; the detection of an amplitude-modulated X-ray standing wave above the surface of a planar X-ray waveguide structure; and the use of this phenomenon for characterization of organic Langmuir–Blodgett films. These results determine the modern level of research of condensed matter by X-ray methods. These methods will be more important in this century in connection with the further development of the synchrotron radiation sources both in the world and, in particular, in Russia and also in connection with the necessity of obtaining structural information on new materials.

ACKNOWLEDGMENTS

This study was supported by the Foundation for Support of Scientific Schools, project no. NSh-14-4.2003.2.

REFERENCES

1. M. V. Kovalchuk and V. G. Kon, Usp. Fiz. Nauk **149** (1), 69 (1986) [Sov. Phys. Usp. **29**, 426 (1986)].
2. A. M. Afanas'ev, P. A. Aleksandrov, and R. M. Imamov, *X-ray Diffraction Diagnostics of Submicron Layers* (Nauka, Moscow, 1989).
3. B. W. Batterman, Phys. Rev. Lett. **22**, 703 (1969); Appl. Phys. Lett. **1**, 68 (1962).
4. B. W. Batterman, Phys. Rev. **133**, 759 (1964).
5. B. W. Batterman, Phys. Rev. Lett. **22**, 703 (1969).
6. J. A. Golovchenko, B. W. Batterman, and W. I. Brown, Phys. Rev. B **10**, 4239 (1974).
7. S. Annaka, S. Kikuta, and K. Kohra, J. Phys. Soc. Jpn. **21**, 1559 (1966).

8. S. Annaka, S. Kikuta, and K. Kohra, J. Phys. Soc. Jpn. **20**, 2093 (1965).
9. V. N. Shchemelev, M. V. Kruglov, and V. P. Pronin, Fiz. Tverd. Tela (Leningrad) **12** (8), 2495 (1970) [Sov. Phys. Solid State **12**, 2005 (1970)].
10. V. N. Shchemelev and M. V. Kruglov, Fiz. Tverd. Tela (Leningrad) **14** (12), 3556 (1972) [Sov. Phys. Solid State **14**, 2988 (1972)].
11. M. V. Kruglov, V. N. Shchemelev, and G. G. Kareva, Phys. Status Solidi A **46**, 343 (1978).
12. M. V. Kruglov, E. A. Sozontov, V. N. Shchemelev, and B. G. Zakharov, Kristallografiya **22** (4), 693 (1977) [Sov. Phys. Crystallogr. **22**, 397 (1977)].
13. A. M. Afanas'ev and V. G. Kon, Zh. Éksp. Teor. Fiz. **74** (1), 300 (1978) [Sov. Phys. JETP **47**, 154 (1978)].
14. V. G. Kohn and M. V. Kovalchuk, Phys. Status Solidi A **64**, 359 (1981).
15. A. M. Afanas'ev and S. L. Azizzyan, Acta Crystallogr., Sect. A: Cryst. Phys., Diffr., Theor. Gen. Crystallogr. **37**, 125 (1981).
16. A. M. Afanas'ev, É. A. Manykin, É. F. Lobanovich, *et al.*, Fiz. Tverd. Tela (Leningrad) **24** (9), 2599 (1982) [Sov. Phys. Solid State **24**, 1473 (1982)].
17. S. I. Zheludeva, M. V. Kovalchuk, and V. G. Kohn, J. Phys. C: Solid State Phys. **18** (11), 2287 (1985).
18. A. M. Afanas'ev, R. M. Imamov, É. Kh. Mukhamedzhanov, and Le Kong Kui, Dokl. Akad. Nauk SSSR **288** (4), 847 (1986) [Sov. Phys. Dokl. **31**, 492 (1986)].
19. A. M. Afanas'ev, R. M. Imamov, É. Kh. Mukhamedzhanov, *et al.*, Dokl. Akad. Nauk SSSR **289** (2), 341 (1986) [Sov. Phys. Dokl. **31**, 562 (1986)].
20. A. M. Afanas'ev, R. M. Imamov, E. Kh. Mukhamedzhanov, and V. N. Peregudov, Phys. Status Solidi A **98**, 367 (1986).
21. V. G. Kon, Fiz. Tverd. Tela (Leningrad) **28** (10), 3028 (1986) [Sov. Phys. Solid State **28**, 1704 (1986)].
22. A. M. Afanas'ev, R. M. Imamov, E. Kh. Mukhamedzhanov, and A. A. Nazlukhanyan, Phys. Status Solidi A **104**, K73 (1987).
23. M. V. Kovalchuk, I. A. Vartanyans, and V. G. Kohn, Acta Crystallogr., Sect. A: Found. Crystallogr. **43** (2), 180 (1987).
24. A. Yu. Kazimirov, M. V. Kovalchuk, and V. G. Kohn, *X-ray and Neutron Structure Analysis in Material Science*, Ed. by J. Hasek (Plenum, New York, 1989), p. 273.
25. A. Yu. Kazimirov, M. V. Kovalchuk, and V. G. Kohn, Acta Crystallogr., Sect. A: Found. Crystallogr. **46**, 643 (1990).
26. A. M. Afanas'ev, R. M. Imamov, and E. Kh. Mukhamedzhanov, Cryst. Rev. **3**, 157 (1992).
27. A. M. Afanas'ev and R. M. Imamov, Kristallografiya **40** (3), 446 (1995) [Crystallogr. Rep. **40**, 406 (1995)].
28. S. I. Zheludeva, M. V. Kovalchuk, N. N. Novikova, *et al.*, Kristallografiya **40** (1), 145 (1995) [Crystallogr. Rep. **40**, 132 (1995)].
29. M. V. Kovalchuk, A. Yu. Kazimirov, V. G. Kohn, and L. V. Samoilova, Physica B (Amsterdam) **221**, 445 (1996).
30. S. I. Zheludeva, M. V. Kovalchuk, N. N. Novikova, *et al.*, J. Appl. Crystallogr. **30**, 833 (1997).
31. S. A. Grigoryan, M. V. Kovalchuk, and V. L. Nosik, Poverkhnost, No. 8, 5 (1999).
32. I. A. Vartanyants and M. V. Kovalchuk, Rep. Prog. Phys. **64**, 1009 (2001).
33. M. V. Kovalchuk, D. Liljequist, and V. G. Kon, Fiz. Tverd. Tela (Leningrad) **28** (11), 3409 (1986) [Sov. Phys. Solid State **28**, 1918 (1986)].
34. A. V. Afanas'ev, R. M. Imamov, E. Kh. Mukhamedzhanov, and A. N. Chuzo, Acta Crystallogr., Sect. A: Found. Crystallogr. **42**, 24 (1986).
35. A. M. Afanas'ev, R. M. Imamov, Z. N. Igamkulov, and É. Kh. Mukhamedzhanov, Kristallografiya **39** (2), 250 (1994) [Crystallogr. Rep. **39**, 209 (1994)].
36. A. M. Afanas'ev and V. N. Peregudov, Dokl. Akad. Nauk SSSR **301** (5), 1098 (1988) [Sov. Phys. Dokl. **33**, 607 (1988)].
37. A. M. Afanas'ev, R. M. Imamov, A. V. Maslov, *et al.*, Dokl. Akad. Nauk SSSR **309** (1), 78 (1989) [Sov. Phys. Dokl. **34**, 997 (1989)].
38. A. M. Afanas'ev, R. M. Imamov, A. V. Maslov, *et al.*, Kristallografiya **36** (2), 513 (1991) [Sov. Phys. Crystallogr. **36**, 283 (1991)].
39. S. M. Durbin, L. E. Berman, and B. W. Batterman, Phys. Rev. B **33**, 4402 (1986).
40. A. M. Afanas'ev, R. M. Imamov, É. Kh. Mukhamedzhanov, and Le Kong Kui, Dokl. Akad. Nauk SSSR **295** (4), 839 (1987) [Sov. Phys. Dokl. **32**, 650 (1987)].
41. A. M. Afanas'ev, R. M. Imamov, E. Kh. Mukhamedzhanov, and A. A. Bzheumikhov, Phys. Status Solidi A **116**, 197 (1989).
42. V. G. Kohn, Phys. Status Solidi A **106** (1), 31 (1988).
43. M. V. Kovalchuk, É. K. Kov'ev, A. V. Mirenskiĭ, and Yu. N. Shilin, Prib. Tekh. Éksp., No. 4, 203 (1975).
44. M. V. Kovalchuk, É. K. Kov'ev, Yu. M. Kozelikhin, *et al.*, Prib. Tekh. Éksp., No. 1, 194 (1976).
45. M. V. Kovalchuk, Yu. N. Shilin, S. I. Zheludeva, *et al.*, Nucl. Instrum. Methods Phys. Res. A **448**, 112 (2000).
46. M. V. Kovalchuk and Yu. N. Shilin, Élektron. Tekh., Ser. Mater., No. 3 (202), 38 (1985).
47. D. A. Bugrov, R. M. Imamov, and É. M. Pashaev, Prib. Tekh. Éksp., No. 2, 203 (1984).
48. M. V. Kovalchuk, S. S. Yakimov, R. M. Imamov, *et al.*, Prib. Tekh. Éksp., No. 6, 185 (1981).
49. R. M. Imamov and É. Kh. Mukhamedzhanov, in *Structural Studies of Crystals* (Nauka, Moscow, 1997), p. 132.
50. M. V. Kovalchuk, A. M. Nikolaenko, A. S. Semiletov, and G. A. Gusev, Prib. Tekh. Éksp., No. 5, 178 (1987).
51. P. A. Aleksandrov, E. E. Bresler, D. A. Bugrov, *et al.*, Prib. Tekh. Éksp., No. 1, 198 (1986).
52. M. V. Kovalchuk, Yu. N. Shilin, A. G. Denisov, *et al.*, Prib. Tekh. Éksp., No. 3, 191 (1987).
53. N. Hertel, M. V. Kovalchuk, A. M. Afanas'ev, and R. M. Imamov, Phys. Lett. A **75A** (6), 501 (1980).
54. É. M. Pashaev, É. Kh. Mukhamedzhanov, and M. V. Kovalchuk, Kristallografiya **28** (5), 1018 (1983) [Sov. Phys. Crystallogr. **28**, 603 (1983)].
55. M. V. Kovalchuk and É. Kh. Mukhamedzhanov, Fiz. Tverd. Tela (Leningrad) **25** (12), 3532 (1983) [Sov. Phys. Solid State **25**, 2033 (1983)].

56. A. M. Afanas'ev, B. G. Zakharov, R. M. Imamov, and M. V. Kovalchuk, Élektron. Prom., Nos. 11(15)–12(96), 47 (1980).
57. B. G. Zakharov, M. V. Kovalchuk, V. G. Kon, and E. A. Sozontov, Élektron. Tekh., Ser. Mater., No. 1 (246), 3 (1990).
58. V. G. Kohn, M. V. Kovalchuk, R. M. Imamov, *et al.*, Phys. Status Solidi A **71**, 603 (1982).
59. B. G. Zakharov, M. V. Kovalchuk, Yu. V. Kovalchuk, *et al.*, Pis'ma Zh. Tekh. Fiz. **10** (22), 1402 (1984) [Sov. Tech. Phys. Lett. **10**, 592 (1984)].
60. B. G. Zakharov, S. S. Strel'chenko, E. A. Sozontov, and M. V. Kruglov, Élektron. Tekh., Ser. Mater., No. 7, 46 (1980).
61. E. A. Sozontov, B. G. Zakharov, and V. M. Ustinov, Élektron. Tekh., No. 4 (89), 35 (1989).
62. E. A. Sozontov, M. V. Kruglov, and B. G. Zakharov, Élektron. Tekh., Ser. Mater., No. 7, 108 (1979).
63. E. A. Sozontov, M. V. Kruglov, and B. G. Zakharov, Phys. Status Solidi A **56**, 303 (1981).
64. M. V. Kovalchuk, V. G. Kon, and É. F. Lobanovich, Fiz. Tverd. Tela (Leningrad) **27** (11), 3379 (1985) [Sov. Phys. Solid State **27**, 2034 (1985)].
65. E. A. Sozontov, M. V. Kovalchuk, B. G. Zakharov, and S. I. Zheludeva, Poverkhnost, Nos. 8–9, 118 (1998).
66. A. M. Afanas'ev, R. M. Imamov, A. V. Maslov, *et al.*, Kristallografiya **38** (3), 58 (1993) [Crystallogr. Rep. **38**, 319 (1993)].
67. A. M. Afanas'ev, R. M. Imamov, A. V. Maslov, and E. V. Pashaev, Phys. Status Solidi A **84**, 73 (1984).
68. R. M. Imamov, É. M. Pashaev, M. N. Abdullaev, and I. R. Nuriev, Fiz. Tverd. Tela (Leningrad) **27** (6), 1631 (1985) [Sov. Phys. Solid State **27**, 982 (1985)].
69. A. M. Afanas'ev, R. M. Imamov, A. V. Maslov, and É. M. Pashaev, Kristallografiya **30** (1), 67 (1985) [Sov. Phys. Crystallogr. **30**, 35 (1985)].
70. A. M. Afanas'ev, R. M. Imamov, E. Kh. Mukhamedzhanov, and Le Kong Kui, Phys. Status Solidi A **92**, 355 (1985).
71. M. V. Kovalchuk and E. Kh. Mukhamedzhanov, Phys. Status Solidi A **81**, 427 (1984).
72. É. Kh. Mukhamedzhanov, A. V. Maslov, A. N. Chuzo, and R. M. Imamov, Poverkhnost, No. 3, 54 (1984).
73. A. V. Maslov, É. Kh. Mukhamedzhanov, Le Kong Kui, and R. M. Imamov, Kristallografiya **32** (3), 723 (1987) [Sov. Phys. Crystallogr. **32**, 424 (1987)].
74. I. A. Vartan'yants, M. V. Kovalchuk, V. G. Kon, *et al.*, Pis'ma Zh. Éksp. Teor. Fiz. **49** (1), 630 (1989) [JETP Lett. **49**, 726 (1989)].
75. M. V. Kovalchuk, N. Hertel, M. K. Melkonyan, *et al.*, Phys. Status Solidi A **66** (1), K173 (1981).
76. A. Yu. Kazimirov and M. V. Kovalchuk, Kristallografiya **32** (3), 730 (1987) [Sov. Phys. Crystallogr. **32**, 428 (1987)].
77. A. Yu. Kazimirov, M. V. Kovalchuk, and V. G. Kon, Pis'ma Zh. Tekh. Fiz. **13** (16), 982 (1987) [Sov. Tech. Phys. Lett. **13**, 409 (1987)].
78. S. I. Zheludeva, B. G. Zakharov, M. V. Kovalchuk, *et al.*, Kristallografiya **33** (6), 1352 (1988) [Sov. Phys. Crystallogr. **33**, 804 (1988)].
79. E. Kh. Mukhamedzhanov, A. V. Maslov, R. M. Imamov, *et al.*, J. Appl. Crystallogr. **24**, 6 (1991).
80. I. A. Vartanyants, M. V. Kovalchuk, A. N. Sosfenov, *et al.*, Acta Phys. Pol. A **80**, 811 (1991).
81. I. A. Vartanyants, M. V. Kovalchuk, and V. M. Beresovskii, Phys. Status Solidi A **135**, 513 (1993).
82. I. A. Vartanyants, M. V. Kovalchuk, and V. M. Beresovskii, J. Phys. D: Appl. Phys. **26**, A197 (1993).
83. I. A. Vartanyants, M. V. Kovalchuk, and V. M. Beresovskii, J. Phys. **4**, PC-9 191-C-9 194 (1994).
84. M. V. Kovalchuk, E. A. Sozontov, and B. G. Zakharov, Poverkhnost, No. 11, 10 (1997).
85. A. Yu. Kazimirov, M. V. Kovalchuk, A. N. Sosfenov, *et al.*, Acta Crystallogr., Sect. B: Struct. Sci. **48**, 577 (1992).
86. S. I. Zheludeva, M. V. Kovalchuk, and S. G. Konnikov, Zh. Tekh. Fiz. **54** (3), 655 (1984) [Sov. Phys. Tech. Phys. **29**, 389 (1984)].
87. S. I. Zheludeva and M. V. Kovalchuk, Fiz. Tekh. Poluprovodn. (Leningrad) **19**, 1597 (1985) [Sov. Phys. Semicond. **19**, 982 (1985)].
88. M. Bedzik, M. V. Kovalchuk, G. Materlik, *et al.*, Dokl. Akad. Nauk SSSR **282** (1), 76 (1985) [Sov. Phys. Dokl. **30**, 381 (1985)].
89. M. V. Kovalchuk, V. G. Kon, and É. F. Lobanovich, Fiz. Tekh. Poluprovodn. (Leningrad) **23** (6), 1054 (1989) [Sov. Phys. Semicond. **23**, 657 (1989)].
90. A. Yu. Kazimirov, M. V. Kovalchuk, and V. G. Kon, Kristallografiya **32** (6), 1360 (1987) [Sov. Phys. Crystallogr. **32**, 799 (1987)].
91. V. A. Bushuev, A. Yu. Kazimirov, and M. V. Kovalchuk, Pis'ma Zh. Éksp. Teor. Fiz. **47** (3), 154 (1988) [JETP Lett. **47**, 187 (1988)].
92. S. A. Grigoryan and M. V. Kovalchuk, Poverkhnost, Nos. 5–6, 119 (1999).
93. S. I. Zheludeva, M. V. Kovalchuk, N. N. Novikova, *et al.*, Pis'ma Zh. Tekh. Fiz. **15** (20), 49 (1989) [Sov. Tech. Phys. Lett. **15**, 808 (1989)].
94. S. I. Zheludeva, M. V. Kovalchuk, S. Lagomarzino, *et al.*, Pis'ma Zh. Éksp. Teor. Fiz. **52** (3), 804 (1990) [JETP Lett. **52**, 170 (1990)].
95. S. I. Zheludeva, M. V. Kovalchuk, N. N. Novikova, *et al.*, Pis'ma Zh. Tekh. Fiz. **16** (14), 37 (1990) [Sov. Tech. Phys. Lett. **16**, 537 (1990)].
96. S. I. Zheludeva, S. Lagomarsino, N. N. Novikova, *et al.*, J. Phys. D: Appl. Phys. **26**, A202 (1993).
97. S. I. Zheludeva, M. V. Kovalchuk, N. N. Novikova, *et al.*, J. Phys. D: Appl. Phys. **26**, A206 (1993).
98. S. I. Zheludeva, M. V. Kovalchuk, N. N. Novikova, *et al.*, Thin Solid Films **232**, 252 (1993).
99. S. I. Zheludeva, M. V. Kovalchuk, N. N. Novikova, *et al.*, Physica B (Amsterdam) **198**, 259 (1994).
100. E. Buratini, G. Cappuccio, S. Simeoni, *et al.*, Synchrotron Radiat. News **6** (5), 16 (1993).
101. S. I. Zheludeva, M. V. Kovalchuk, N. N. Novikova, *et al.*, Thin Solid Films **259**, 131 (1995).
102. M. V. Kovalchuk and S. I. Zheludeva, J. Phys. **4**, C9431 (1994).
103. S. I. Zheludeva, M. V. Kovalchuk, N. N. Novikova, *et al.*, J. Phys. **4**, 1581 (1994).

104. E. Burattini, G. Cahhuccio, V. Sessa, *et al.*, Mater. Sci. Forum **166–169**, 337 (1994).

105. S. I. Zheludeva, M. V. Kovalchuk, N. N. Novikova, *et al.*, Mater. Sci. Eng. **3**, 181 (1995).

106. S. I. Zheludeva, M. V. Kovalchuk, N. N. Novikova, and A. N. Sosfenov, Adv. X-Ray Chem. Anal., Jpn. **26**, 181 (1995).

107. S. I. Zheludeva, M. V. Kovalchuk, N. N. Novikova, *et al.*, Kristallografiya **40** (1), 145 (1995) [Crystallogr. Rep. **40**, 132 (1995)].

108. S. I. Zheludeva, M. V. Kovalchuk, N. N. Novikova, *et al.*, Thin Solid Films **259**, 131 (1995).

109. S. I. Zheludeva, M. V. Kovalchuk, N. N. Novikova, *et al.*, J. Appl. Crystallogr. **30**, 838 (1997).

110. S. I. Zheludeva and M. V. Kovalchuk, Poverkhnost, Nos. 8–9, 122 (1998).

111. S. I. Zheludeva, M. V. Kovalchuk, and N. N. Novikova, Spectrochim. Acta B **56**, 2019 (2001).

112. V. G. Kohn, Fiz. Tverd. Tela (Leningrad) **28** (10), 3028 (1986) [Sov. Phys. Solid State **28**, 1704 (1986)].

113. V. G. Kohn, Phys. Status Solidi A **106** (1), 31 (1988).

114. M. V. Kovalchuk, I. A. Vartanyants, and V. G. Kohn, Acta Crystallogr., Sect. A: Found. Crystallogr. **43** (2), 180 (1987).

115. A. Yu. Kazimirov, M. V. Kovalchuk, V. G. Kohn, *et al.*, Photon Factory Utility Rep., No. 9, 239 (1991).

116. A. Yu. Kazimirov, M. V. Kovalchuk, V. G. Kohn, *et al.*, Photon Factory Utility Rep., No. 9, 240 (1991).

117. V. G. Kon and L. V. Samoĭlova, Kristallografiya **36** (1), 25 (1991) [Sov. Phys. Crystallogr. **36**, 11 (1991)].

118. V. G. Kohn and L. V. Samoilova, Phys. Status Solidi A **133** (1), 9 (1992).

119. A. Yu. Kazimirov, M. V. Kovalchuk, V. G. Kohn, *et al.*, Phys. Status Solidi A **135** (6), 507 (1993).

Translated by L. Man